

Modeling the spatiotemporal dynamics of global electric power consumption (1992–2019) by utilizing consistent nighttime light data from DMSP-OLS and NPP-VIIRS

Ting Hu^a, Ting Wang^b, Qingyun Yan^a, Tiexi Chen^c, Shuanggen Jin^{a,d,e,*}, Jun Hu^f

^a School of Remote Sensing and Geomatics Engineering, Nanjing University of Information Science and Technology, Nanjing 210044, PR China

^b Department of Natural Resources of Hubei Province, Wuhan 430079, PR China

^c School of Geographical Science, Nanjing University of Information Science and Technology, Nanjing 210044, PR China

^d Shanghai Astronomical Observatory, Chinese Academy of Sciences, Shanghai 200030, PR China

^e School of Surveying and Land Information Engineering, Henan Polytechnic University, Jiaozuo 454000, PR China

^f Maintenance Technology Center, Jiangxi Provincial Communications Investment Group Co., Ltd. Road Network Operation Management Company, PR China

HIGHLIGHTS

- The dataset of built-up area density outperforms NDVI in tackling saturation issue of DMSP data.
- Inter-annual correction is necessary to remove the discontinuity effect in VIIRS data.
- A two-step regression-based method is developed to synthesize consistent global NTL dataset.
- The spatiotemporal dynamics of global EPC in the recent decade (2010–2019) are investigated.

ARTICLE INFO

Keywords:

Electric power consumption
Consistent nighttime light data
Global spatiotemporal dynamics
Locally adaptive selection
Built-up area density

ABSTRACT

Adequate and up-to-date knowledge of the spatiotemporal dynamics of electricity power consumption (EPC) is important for the sustainable use of global electricity power resources. However, global EPC patterns were not clear after Defense Meteorological Satellite Program Operational Linescan System (DMSP-OLS) in 2013 due to the significant differences between Suomi National Polar-orbiting Partnership Visible Infrared Imaging Radiometer Suite (NPP-VIIRS) and DMSP-OLS. In this paper, global EPC patterns in the recent decade are investigated and assessed for the first time by the proposed locally adaptive method with integrating two nighttime light (NTL) images to global pixel-level EPC from 1992 to 2019. The geospatial dataset of built-up area density (BUAD) is adopted with a higher spatial resolution and more direct relation to human activities. A two-step regression method is designed to simulate DMSP-like images after 2013, based on the inter-annual relationships of provincial-level VIIRS. With this consistent nighttime light dataset, pixel-level EPC over the 28 years are estimated for the first time, and then the spatiotemporal dynamics of EPC are investigated from global, continental, to national scales. The obtained EPC estimates are of satisfactory accuracy in 92.6% of the countries with a MARE (Mean of the Absolute Relative Error) of less than 20%. Over these 28 years, Japan, South Korea, and China experienced high proportion of EPC high-growth. These results provide reliable scientific basis for exploring the spatial pattern and temporal variations of global EPC, especially for the latest years.

1. Introduction

Continuing urbanization and industrialization are causing a dramatic increase in energy consumption and carbon dioxide emissions, and growing energy shortages and global warming [1]. For the sake of

resisting global climate change, more than 120 countries/regions worldwide have proposed carbon neutrality targets, including the European Union, the United States, Canada, Japan and China [2]. Being a fundamental component of the quality of life in modern society, electricity plays an influential role in extensive human activities, such as

* Corresponding author.

E-mail address: sgjin@nuiist.edu.cn (S. Jin).

manufacturing and household living and commercial transactions [3–5]. The remarkable growth of electric power consumption (EPC) during the last four decades has accelerated global warming and climate change. Projections for the future suggest that the placement of low-carbon technologies in the power sector could contribute significantly to emission reductions [6]. Therefore, an accurate estimation and better understanding of the spatiotemporal patterns of global EPC are essential for policy makers to draw up energy efficiency and emission reduction plans [7]. However, the traditional data sources of EPC are census statistics at the administrative unit level (e.g., city), which are time-lagging and spatial-inexplicit. What's worse, there are not any available censuses in some developing areas [8].

Numerous efforts have been made to estimate EPC at different geographical scales, by utilizing other supplements. Al-Garni et al. [9] completed the EPC forecasting in Eastern Saudi Arabia with the assistance of demographical variables and meteorological data. Shiu and Lam [10] focused on the causal relationship between EPC and real Gross Domestic Product (GDP) in China through error-correction model. Deng et al. [11] utilized social media data as a proxy to estimate the EPC at the building level. Wang et al. [12] proposed matching and machine-learning methods to synthesize available statistics to produce household energy distribution and estimate residential energy consumption at a neighborhood scale. The abovementioned studies yielded reasonable results, however, these EPC estimates can hardly be spatialized due to the coarse resolution of the independent variables [13]. Moreover, the heavy economic burden restricts the spatial and temporal coverages of statistics data, making it difficult to support large-scale or even worldwide estimation [14].

Orbiting satellites constantly observe the Earth in a preprogrammed manner and hence obtain periodic gridded images. The nighttime light (NTL) remote sensing imagery from the Defense Meteorological Satellite Program's Operational Linescan System (hereafter referred to DMSP) has played an indispensable role in the estimation of various socio-economic parameters, such as GDP, population, human well-being, and EPC [15–18]. The general idea is to find regression models to establish the relationship between NTL and EPC. Regression methods can be divided into two main categories, namely the global regression and the grouping one, based on the spatial heterogeneity of these models.

The global regression refers to that the EPC-NTL relationship remains consistent across the entire study area, and thus the use of only one model is sufficient. Owing to the simplicity of global model, it is the most frequently employed in the literatures. Elvidge et al. [19] discovered a strong log-log association between EPC and illuminated regions in DMSP images. Amaral et al. [15] utilized linear model to relate EPC and lit areas from DMSP in the urban settlements of Brazilian Amazonia. Letu et al. [20] observed the linear correlation between saturated-corrected DMSP intensities and EPC in Japan, India and China. Townsend and Bruce [21] established the relationship between DMSP NTL and EPC through a second-order polynomial model across Australia for 1997–2002. Regarding pixel-level EPC mapping, Zhao et al. [22] designed a single model to generate pixel-level EPC map throughout China, utilizing DMSP and urban population data. Cao et al. [23] obtained a statistical model using DMSP brightness and population as independent variables, and then applied it to the grid level to produce 1-km-resolution EPC map in China. He et al. [24] adopted linear function to complete the pixel-level EPC mapping in Mainland China (2000–2008). Moreover, some complex global regression models have also been applied to estimate higher-accuracy EPC. For instance, Jasinski [25] found that the use of artificial neural networks could credibly model the non-linear relations among EPC, NTL, normalized difference vegetation index (NDVI), and built-up areas.

The grouping type means that the EPC-NTL relationship is not consistent across the study area, since the spatial heterogeneity cannot be ignored. Xie and Weng [26] designed provincial level model using DMSP, population, and enhanced vegetation index (EVI), with the

difference between urban cores and suburban areas considered. Shi et al. [27] partitioned the world into 48 regions according to geographical distance and development status, and then established individual linear model for each region to explore EPC, based on corrected DMSP data. Xiao et al. [28] developed spatiotemporal geographically weighted regression models to estimate provincial energy consumption in China based on DMSP, with the spatiotemporal differences of the EPC-NTL relationship fully considered. Similar to [27], Lu et al. [29] classified the globe into 6 regions and respectively established linear model between NTL and EPC for each region, after the DMSP NTL data were adjusted by Global Human Settlement Layer (GHSL) and Gridded Population Density data (GPW V4). Li et al. [30] divided Chinese cities into 3 categories using statistical employment data, and then constructed linear weighted regression model for each city type to model pixel-level EPC. Wang and Lu [31] adopted multi-scale geographically weighted regression model to estimate city-level EPC in China, taking the land use types and landscape patterns into account. Another related work using grouping-type-method is the authors' previous research [32], where a locally adaptive method in the selections of NTL data correction and regression model was proposed to consider socioeconomic inconsistencies. However, all these works almost have not focused on EPC estimation at the global level.

Significant geospatial heterogeneity in the world makes the practice of grouping-type-method exclusive, as in [27], [29] and [32]. However, it is noteworthy that these explorations of EPC modeling only extend to 2013, which is the final year of DMSP data available. The gridded EPC data from nearly 10 years ago cannot support studies of recent years or longer time spans [33]. As the successor to DMSP, the global Suomi National Polar-orbiting Partnership Visible Infrared Imaging Radiometer Suite (hereafter referred to as VIIRS) is still active in providing on-board calibrated NTL imagery with higher spatial resolution (500/740 m) and radiometric resolution (12/14 bit) [34]. The cross-sensor calibration of these two generations of NTL imagery should be carefully designed to cope with their inconsistencies, and only then can a long time-series (especially after 2013) of pixel-level EPC product be well established worldwide. Researchers have made some investigations to generate an integrated nighttime light dataset based on DMSP and VIIRS [35]. Zhu et al. [36] discovered the power function relationship between the total brightness of DMSP and VIIRS at the provincial scale, and then generated DMSP-like NTL data based on the cumulated VIIRS NTL intensity in China. Li et al. [37] also utilized power function to intercalibrate DMSP and VIIRS for the analysis of human settlement loss in Syria. Zheng et al. [38] proposed a geographically weighted regression model based on DMSP and VIIRS data and then produced simulated DMSP NTL data from 2014 to 2017 in China. Zhao et al. [39] initially conducted a set of preprocess procedures and then designed a sigmoid regression model to simulate the DMSP-like NTL data in Southeast Asia. Li et al. [40] released an annual harmonized nighttime light dataset from 1992 to 2018, utilizing kernel density method and sigmoid function to convert VIIRS to the DMSP-like NTL data (2014–2018). In contrast to generate DMSP-like NTL, Chen et al. [41] trained an auto-encoder model based on the enhanced DMSP and VIIRS in 2013, and then applied the trained model to simulate VIIRS-like NTL data in 2000–2012, and finally produced the extend time series (2000–2018) of VIIRS-like NTL. These investigations have all made good attempts at constructing time-extended NTL datasets. However, their applicability and effectiveness to map global EPC have yet to be verified. The local-adaptive method proposed in [32] has demonstrated its superiority in global EPC mapping. Therefore, on the basis of local-adaptive method, this research focuses on the integration of DMSP-OLS (DMSP) and NPP-VIIRS (VIIRS) to achieve accurate and up-to-date global EPC mapping. The main contributions are listed as follows.

- 1) The DMSP de-saturation process was conducted with the assistance of NDVI [32], assuming that urban surfaces are inversely correlated with vegetation cover. However, this assumption does not always hold true, such as in arid regions [42]. Population density (e.g., GPW v3/

v4) is another popular choice to solve the saturation issue of DMSP [26,29], however, the time interval of GPW dataset is usually 5 years, directly hindering the accuracy of DMSP correction. In contrast, the built-up area density (BUAD), a surface parameter that can be obtained from remote sensing imagery, has been intensively studied, and a number of global long time-series annually datasets are publicly available [43–46]. Furthermore, the BUAD can reflect the intensity of human activities more intuitively than vegetation (e.g., NDVI). Therefore, a direct indicator of urban surfaces, namely BUAD, is employed to deal with the DMSP saturation issue in this work.

2) Due to the sensor upgrades, VIIRS data no longer suffer from saturation and incomparability issue. The VIIRS correction mainly focuses on the noise removal [17,40,41,47]. However, when using time-series VIIRS, the inter-annual discontinuity effect is rarely taken into account, with one exception that Lv et al. [48] performed the same forward continuum correction for VIIRS in China as for DMSP. Nonetheless, the result in [32] has indicated that different inter-annual correction approaches should be applied in regions with diverse socio-economic status. Therefore, three directions (forward, backward, and average) are considered as options for the inter-annual correction of global VIIRS data in this research.

3) Although EPC patterns have been explored extensively, the spatiotemporal dynamics of global EPC from a long-term perspective, particularly in the last decade, remains unknown. To fill this void and refer to the fruits of scholars, this study designs a regression-based scheme to generate DMSP-like images (2014–2019), based on the inter-annual relationships of provincial-level VIIRS. With this consistent global NTL dataset (1992–2019), the first 1-km gridded dataset of global electricity power consumption over the recent 28 years is produced, and used as a basis to analyze global EPC spatiotemporal dynamics at global, continental, and national levels.

2. Datasets

The data sources mainly include DMSP, VIIRS, global impervious surface area (GISA) dataset, global EPC statistics, and administrative boundaries (Table 1). Details of these data sources are elaborated below.

The Version 4 global nighttime stable light (NSL) data of DMSP from different satellites (F10, F12, F14, F15, F16, and F18) were employed as the annual DMSP NTL composites in 1992–2013, acquired from the National Oceanic and Atmospheric Administration-National Geophysical Data Center (NOAA/NGDC) website (<http://www.ngdc.noaa.gov/eog/dmsp.html>). This NSL dataset covers nearly the globe, from 180°W–180°E in longitude and 65°S–75°N in latitude, with a resolution of 30 arc-second. The NSL imagery uses integers from 0 to 63 to reflect the difference of brightness on the Earth's surface. Another DMSP image downloaded from the same website is the global radiance-calibrated nighttime light (RCNL) image in 2006, which was used to address the

incomparability issue of NSL data, as well as to evaluate the effect of saturation correction.

The Version 1 suite of monthly cloud-free VIIRS composite images in 2013–2019 were collected from Earth Observation Group (EOG) official website (<https://eogdata.mines.edu/products/vnl>). This VIIRS product has a spatial resolution of 15 arc-second, recording the light intensity in radiance units (W/cm²/sr). The configuration used in this work is the monthly “VIIRS Cloud Mask (vcm)”, which excludes any data impacted by stray light. On the basis of the monthly VIIRS dataset, we performed annual composition process, referring to the weighting average method in Li et al. [40]. The resulting annual VIIRS dataset can remain satisfactory quality, even in middle/high-latitude-cities. Noise removal is a requisite part of annual VIIRS image pre-processing [17,40,41,47]. According to Li et al. [40], in the regions between 45°S and 45°N, radiances below 0.3×10^{-9} W/cm²/sr were masked to remove dim light noises from temporal lights; for the areas impacted by the aurora (below 45°S or above 45°N), radiances lower than 1.5×10^{-9} W/cm²/sr were excluded.

The website (https://irsip.whu.edu.cn/resources/resources_en_v2.php) [46] provides global impervious surface area (GISA) dataset (1972–2019) with a resolution of 30 m, which is by far the most accurate built-up area (BUA) product with an overall accuracy of over 95%. Since the GISA product indicates whether a pixel (30 m × 30 m) belongs to BUA, we counted the number of BUA pixels in each 1 km × 1 m grid per year and obtained the 1-km-resolution maps of built-up area density (BUAD) during 1992–2019. The values of BUAD range from 0 to 1. Larger values denote more built-up areas distributed in a 1 km × 1 km grid. The annual DMSP NSL, DMSP RCNL, VIIRS, and BUAD images were all resampled to the size of 1 km on Mollweide projection.

The annual global EPC statistics for the countries/districts were obtained from the World Bank Open Database (<https://data.worldbank.org/>), and the specific steps are detailed in Section Appendix. A query in September 2021 found that, the most recent data available in this database were only up to 2014, which shows the heavy cost of census collecting. We downloaded the continent and country boundary data from the Version 3.6 Database of Global Administrative Areas (GADM, <http://gadm.org/>). In addition, Landsat 5 TM images were obtained from the United States Geological Survey (USGS, <https://earthexplorer.usgs.gov/>), in order to assess the performance of DMSP NSL saturation correction.

3. Methodology

Taking our previous work [32] as a basis, this paper embedded the correction of VIIRS and the integration of two NTL datasets into the locally-adaptive framework, to produce 1-km-resolution global gridded EPC maps during 1992–2019. Fig. 1 demonstrates the five major procedures: 1) disaggregation of global NTL (including DMSP and VIIRS) into national NTL data based on country/district boundaries; 2) construction of all possible options in both the processes of NTL (including DMSP and VIIRS) correction and regression model, to form candidate processing chains for each country/district; 3) country/district-wise adaptive selection of the optimal processing chain; 4) assessment of the global EPC (1992–2019) product; 5) spatiotemporal analysis of global EPC during 1992–2019 and 2010–2019.

3.1. Construction of candidate processing chains (model steps 1–4)

The processing chain for pixel-level EPC estimation for each country/district consists of these four steps: (i) DMSP NSL data correction, (ii) annual VIIRS data correction, (iii) integration of corrected DMSP NSL and VIIRS, and (iv) establishment of EPC-NTL regression model. As Fig. 1 shows, there are a different number of options in each step. Concatenating the selected option in each step created a possible processing chain.

Table 1
Description of the utilized datasets in this paper.

Data	Data description	Source
DMSP NSL	Annual nighttime stable light composites for 1992–2013	NOAA/NGDC
DMSP RCNL	Global radiance-calibrated nighttime light image in 2006	NOAA/NGDC
VIIRS	Annual composites of monthly VIIRS for 2013–2019	EOG
BUAD	Annual maps of built-up area density from 1992 to 2019	Wuhan University
Statistical EPC Boundaries	Annual EPC statistics from 1992 to 2014	World Bank Open Database
Boundaries	Shapefile of global continents and countries (v3.6)	Global Administrative Areas
Landsat 5 TM	Images covering representative cities from countries located in different continents	USGS

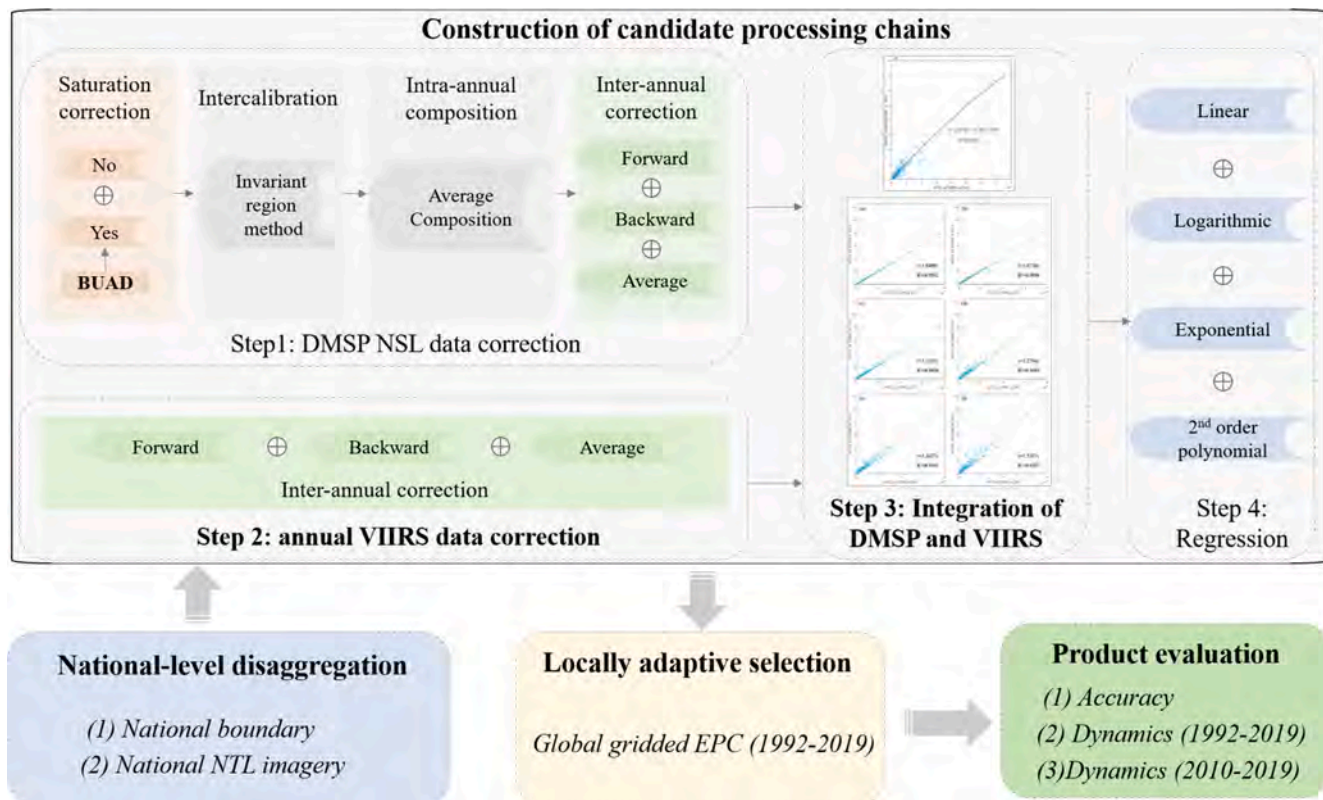


Fig. 1. Flowchart of modelling global EPC dynamics from 1992 to 2019.

3.1.1. DMSP NSL data correction

Due to the low radiometric resolution of DMSP, saturation issue often exists in the urban cores. Considering that urban surfaces are directly correlated with nighttime light, the dataset of built-up-area density (BUAD), which was derived from global impervious surface area (GISA) product, was employed to process these saturated pixels. Furthermore, it is worth noting that saturation correction is not necessary for unsaturated pixels in the suburbs [32,49]. Hence, two options (i.e., Yes and No) were set in the saturation correction routine. If option ‘Yes’ was selected, saturation correction was then conducted according to Eq. (1):

$$\text{scNSL} = \text{BUAD} \times \text{NSL} \quad (1)$$

where the value of BUAD ranges from 0 to 1, and scNSL denotes the saturation-correction NSL. While option ‘No’ was chosen, the original NSL values remained. The advantage of BUAD dataset was analyzed in Section 4.1 and Section 4.2.

The next three procedures of DMSP NSL data correction were intercalibration, intra-annual composition, and inter-annual correction, respectively.

1) Intercalibration aimed to eliminate the incomparability effect resulted from the absence of onboard calibration and sensor degradation, and the popular Invariant Region (IR) method [26,27,29,48] were utilized to acquire global inter-calibrated NSL and scNSL images (1992–2013) (see Appendix for more details).

2) Intra-annual composition was designed to merge the two available images during the same year for some years, and the specific implementations were elaborated in the Appendix.

3) The last procedure, i.e., inter-annual correction, intended to alleviate the abnormal fluctuations among annual NTL observations after the above procedures. Referring to the assumption that the intensity of lit pixels should present a non-declining trend year over year [27,32,48,50], the formula in Eq. (2) was adopted:

$$DN_{(k,i)}^{\text{inter}} = \begin{cases} 0 & DN_{(k+1,i)} = 0 \\ DN_{(k-1,i)} & DN_{(k+1,i)} > 0 \text{ and } DN_{(k-1,i)} > DN_{(k,i)} \\ DN_{(k,i)} & \text{otherwise} \end{cases} \quad (2)$$

where $DN_{(k-1,i)}$, $DN_{(k,i)}$, and $DN_{(k+1,i)}$ are pixel i 's DN values from NSL (or scNSL) images of years $k-1$, k , and $k+1$; $DN_{(k,i)}^{\text{inter}}$ is pixel i 's DN value after inter-annual correction for year k . Please notice that there is another implicit parameter in Eq. (2), that is, the base year of inter-annual correction. The result of Eq. (2) is actually sensitive to this parameter. If we set the first year (i.e., 1992) as the base year, the Eq. (2) indicated a forward correction direction; while the last available year (i.e., 2013) was considered as the base year, a backward direction was conducted. Another possible option was the average of the forward and backward directions [51], which can smooth the possible bias. Therefore, this NSL inter-annual correction part contained three possible options.

3.1.2. Annual VIIRS data correction

VIIRS imagery survives from the problems of saturation or incomparability in DMSP data, owing to the sensor upgrades. Therefore, the first three procedures (saturation correction, intercalibration and intra-annual composition) of DMSP correction are not necessary for the correction of VIIRS data. However, discontinuity effect is still present in the inter-annual observations of VIIRS (see Section 4.1.2 for details), likely due to image quality variations caused by physical parameters such as lunar zenith angle [52] and viewing angle [53]. Therefore, continuous correction (i.e., inter-annual correction) for annual VIIRS data was also conducted as Eq. (2). Similarly, the base year implicit in Eq. (2) can be set differently, bringing three options (forward/backward/average) to this step. However, to lower the model complexity and ensure that VIIRS has the same temporal trend as DMSP, the inter-annual correction direction of VIIRS was set to be consistent with DMSP (identical green color is used in Fig. 1 to indicate this processing principle). Therefore, in effect, only one option was provided in the

VIIRS data correction step.

At this stage, six DMSP NSL datasets (1992–2013), obtained through different selections in saturation correction (with or without BUAD) and the mode of inter-annual correction (forward, backward or average), were prepared for integration with VIIRS (2013–2019).

3.1.3. Integration of DMSP and VIIRS

The overlapping observation periods of DMSP and VIIRS offer the possibility of their integration. In this study, the VIIRS and DMSP images of the common year (i.e., 2013) were selected to explore the relationship between them. To overcome the difference in NTL detection parameters, a two-step regression-based approach was adopted to improve the consistency between DMSP and VIIRS data [48,50].

Initially, the sum of NTL DN values (SNTL) of DMSP and VIIRS data in 2013 were aggregated at the provincial/state level, which is the Level-1 subdivision unit in GADM dataset. The regression fitting results (Fig. 2) showed that the relationship between SNTL of DMSP and SNTL of VIIRS can be modeled as a second-order polynomial function with a coefficient of determination (R^2) as high as 0.8982 (p -value < 0.01), confirming that this model is globally applicable for the integration of DMSP and VIIRS.

Subsequently, we discovered that there were high correlations between provincial SNTL values of VIIRS in 2014–2019 and that of VIIRS in 2013, with R^2 successively decreasing from 0.9952 to 0.9207 (Fig. 3). That is, the further away the target year is from 2013, the lower the corresponding R^2 . It is possibly caused by the sensor degradation and changes in imaging conditions. Actually, it can be found that similar declines of R^2 also occurred in the relevant researches which focused on simulating DMSP-like data of China [48,50].

Therefore, the slopes in these linear functions were respectively employed to generate DMSP-like images for years after 2013, with the DMSP in 2013 as the base. This step can be formulated as Eq. (3):

$$\text{simuDMSP}_k = \text{slope}_k \times \text{DMSP}_{2013} \quad (3)$$

where DMSP_{2013} refers to the DMSP image in 2013, and slope_k denotes the slope between year k ($k = 2014, 2015, \dots, 2019$) and 2013, and simuDMSP_k represents the simulated DMSP images in year k . In this way, six optional time-series-extended nighttime light datasets (1992–2019) were respectively produced by the integration of DMSP and VIIRS.

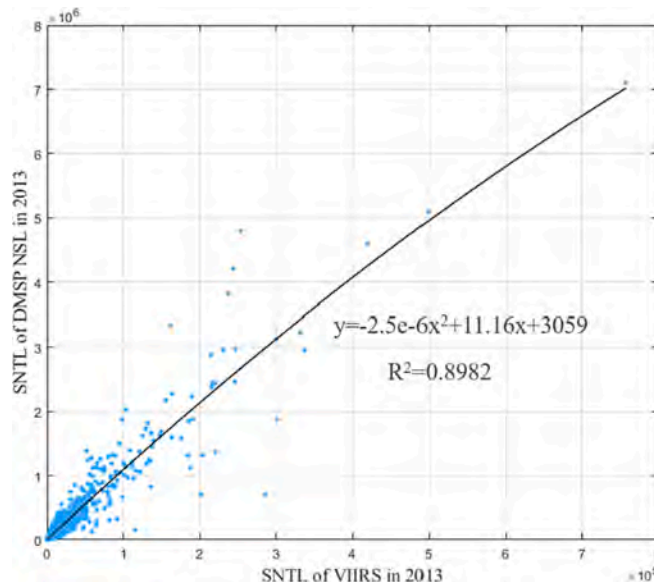


Fig. 2. Relationship between the SNTL of corrected DMSP NSL and VIIRS in 2013.

3.1.4. EPC-NTL regression model

As stated in previous studies [32,54], the type of relationship between EPC and NTL varies from region to region, owing to the different socioeconomic dynamics inherent. Therefore, we set up four optional regression models (i.e., linear, exponential, logarithmic, and second-order polynomial types) to build the relationship between EPC and NTL. These four models are explained as follows:

1) The linear function was applicable when the EPC showed a constant proportional change in response to intensity change in NSL.

2) The concave exponential function assumed that the response rate of EPC gradually increased with the growth of NSL intensity.

3) The convex logarithmic function represented the status that the response rate of EPC gradually increased with the rise of NSL intensity. The EPC would reach a saturated level when sufficient lights were captured.

4) The quadratic term coefficient of the second-order polynomial function determined its concavity/convexity. A positive/negative coefficient denoted the increase/decrease in the response rate to the rise in NSL intensity, respectively.

The estimation of pixel-level EPC was driven by the hypothesis that the relationship F between EPC and NTL for each pixel within a country/district was consistent during the study period [26,27,29]. For the implementation details of these four optional regression models, please refer to the Appendix. Using the statistical EPC and the consistent NTL data from 1992 to 2019, the country-wise coefficients for each regression type were separately solved.

Combining the six options for the NTL data correction (steps 1–3) and four alternatives for the regression model (step 4), there were a total of 24 candidate treatment chains for the EPC estimates of every country/district.

3.2. Locally adaptive selection for EPC estimates

This procedure aimed to choose the best strategy for each country/district among the above-constructed 24 candidate processing chains. According to [32], we adopted R^2 (a measure of goodness-of-fit) as the criteria to assess whether a model is the optimal one or not. That is, the processing chain of the highest R^2 was picked out for the EPC estimates of every country/district.

Additionally, it should be noticed that the World Bank's archived statistics in some countries are not complete or even scarce. Therefore, for the countries/districts with no more than five observations, the proposed locally adaptive method would not be applied. Instead, their models were replaced by models of countries/districts with sufficient statistical EPC from the same region division [27]. Thereby, we produced national 1-km-resolution EPC maps and then pieced them together to generate global pixel-level EPC maps from 1992 to 2019.

3.3. Evaluation of time-series-extended gridded EPC product

For a global geospatial product, the first task that needs to be cared is its accuracy. Therefore, we evaluated the accuracy of the generated EPC maps 1992–2019 at the global, continental, and national levels, using R^2 , RE (Relative Error), and MARE (Mean of the Absolute Relative Error) as indicators, respectively.

To investigate the spatial patterns of global EPC over the 28 years, average EPC map was calculated by averaging annual EPC maps from 1992 to 2019. The map was subsequently classified into five grades: low ($0, 2 \cdot 10^5 \text{ kWh}$), relatively-low ($2, 10 \cdot 10^5 \text{ kWh}$), medium ($10, 40 \cdot 10^5 \text{ kWh}$), relatively-high ($40-200 \cdot 10^5 \text{ kWh}$), and high ($> 200 \cdot 10^5 \text{ kWh}$). Analogously, to explore the temporal variations of global EPC, the difference between the global pixel-level EPC maps in 1992 and 2019 was derived. The difference map was also divided into five grades: no-obvious-growth ($0, 2 \cdot 10^5 \text{ kWh}$), low-growth ($2, 10 \cdot 10^5 \text{ kWh}$), moderate-growth ($10, 40 \cdot 10^5 \text{ kWh}$), relatively-high-growth ($40, 200 \cdot 10^5 \text{ kWh}$), and high-growth ($> 200 \cdot 10^5 \text{ kWh}$). Both the spatial and

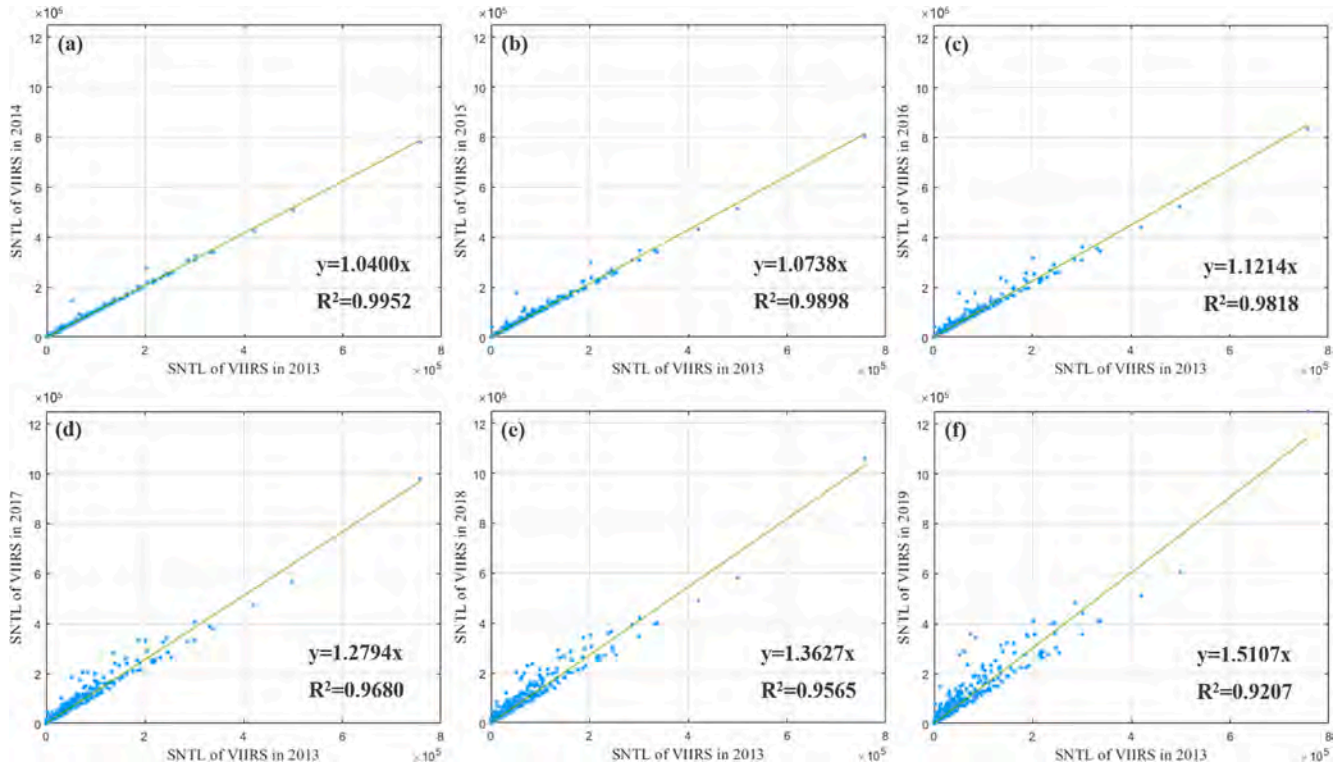


Fig. 3. Linear relationships between the provincial SNTL values of VIIRS in two different years of (a) 2013 and 2014; (b) 2013 and 2015; (c) 2013 and 2016; (d) 2013 and 2017; (e) 2013 and 2018; (f) 2013 and 2019.

the temporal analysis was carried at the global, continental, and national levels, respectively.

Furthermore, we focused on the global EPC dynamics in the recent decade. Specifically, the pixel-level EPC were aggregated to the provincial/state level. Both the global and local Moran's I indices were adopted to portray the worldwide spatial patterns, where the former denotes the overall spatial correlations and the latter characterizes the spatial clustering patterns of provincial EPC. Higher global Moran's I value stands for higher level of spatial autocorrelation [55]. As for local Moran's I , four distinguished types('High-High'/'Low-Low'/'High-Low'/'Low-High') represents different patterns of spatial aggregation [56]. In addition, the *SLOPE* index were utilized to monitor the temporal trends of provincial-level EPC from 2010 to 2019 [57]. Based on the natural break method, the *SLOPE* values at provincial-level were divided into five grades (slow, relatively slow, moderate, relatively rapid, and rapid), to examine the spatial distribution of global EPC growth pace in the recent decade.

4. Results

4.1. Evaluation of corrected nighttime light data

To fully evaluate the results of using built-up area density (BUAD) to correct DMSP data, the regions that suffer from varying degrees of saturation (i.e., different urbanization levels) should be chosen for the comparison. Also, taking the impact of potential climate environment into consideration, five cities (Beijing, Los Angeles, Moscow, Melbourne, and Johannesburg) located in different continents were selected as representatives. In Fig. 4, the VANUI (Vegetation Adjusted Normalized Urban Index) denotes the images that saturation phenomenon was corrected by vegetation [32,58]; the RCNL stands for official offerings without saturation in 2006; the 30-m resolution Landsat 5 TM images in the same year were provided as the reference to show urban regions. Apparently, VANUI images shows less saturation and blooming effects than the original DMSP data in each city. However, the blooming effect

(NTL can be observed in water and soil surfaces) and the indistinguishable intra-urban variability in VANUI images are still relatively serious, compared with RCNL images. Furthermore, the vegetation dataset to construct VANUI is about 6-km-resolution, leading to obvious artifacts in some VANUI images (e.g., Los Angeles, Melbourne, and Johannesburg). In contrast to VANUI, the saturation-corrected DMSP data using BUAD in Fig. 4 (d) are in a high degree of agreement with the spatial patterns of the RCNL and Landsat 5 TM images. The highly accurate annual GISA product provides a reliable density distribution of built-up areas, which in turn greatly reduces the saturation and blooming effects of the original DMSP. Therefore, using built-up area density, rather than the commonly used vegetation data, provides a more satisfactory saturation correction for NTL observations. The visual comparisons in more cities with different urbanization levels and distinct geographical locations are also presented in Fig. E1 of the Appendix.

In addition to DMSP, the VIIRS data also need to be corrected. Fig. 5 displays the sums of annual VIIRS data for four countries with diverse geographical location and socioeconomic status (Algeria, Bangladesh, Brazil, and Italy), and oscillation phenomenon can be clearly observed in each blue curve, implying the necessity of inter-annual correction. The sums of the corrected VIIRS data related to different directions (forward, backward, and average) are also plotted in Fig. 5. For each country, the discontinuity are no longer present in all the three corrected curves, indicating that all three directions could be adopted for inter-annual correction. A more consistent temporal pattern would contribute to the reliability of subsequent EPC estimates [27,32,59].

After correcting DMSP and VIIRS separately, we adopted a regression-based method to simulate global pixel-level DMSP-like dataset from 2014 to 2019, achieving consistent NTL dataset. Fig. 6 shows the sums of pixel-level NTL in four countries (i.e., Algeria, South Korea, Brazil, and Italy) from 1992 to 2019, where the values in 1992–2013 were calculated directly from the DMSP data, and the values in 2014–2019 were from the simulated DMSP-like data. It can be observed that the sums of NTL for all countries are in the trend of

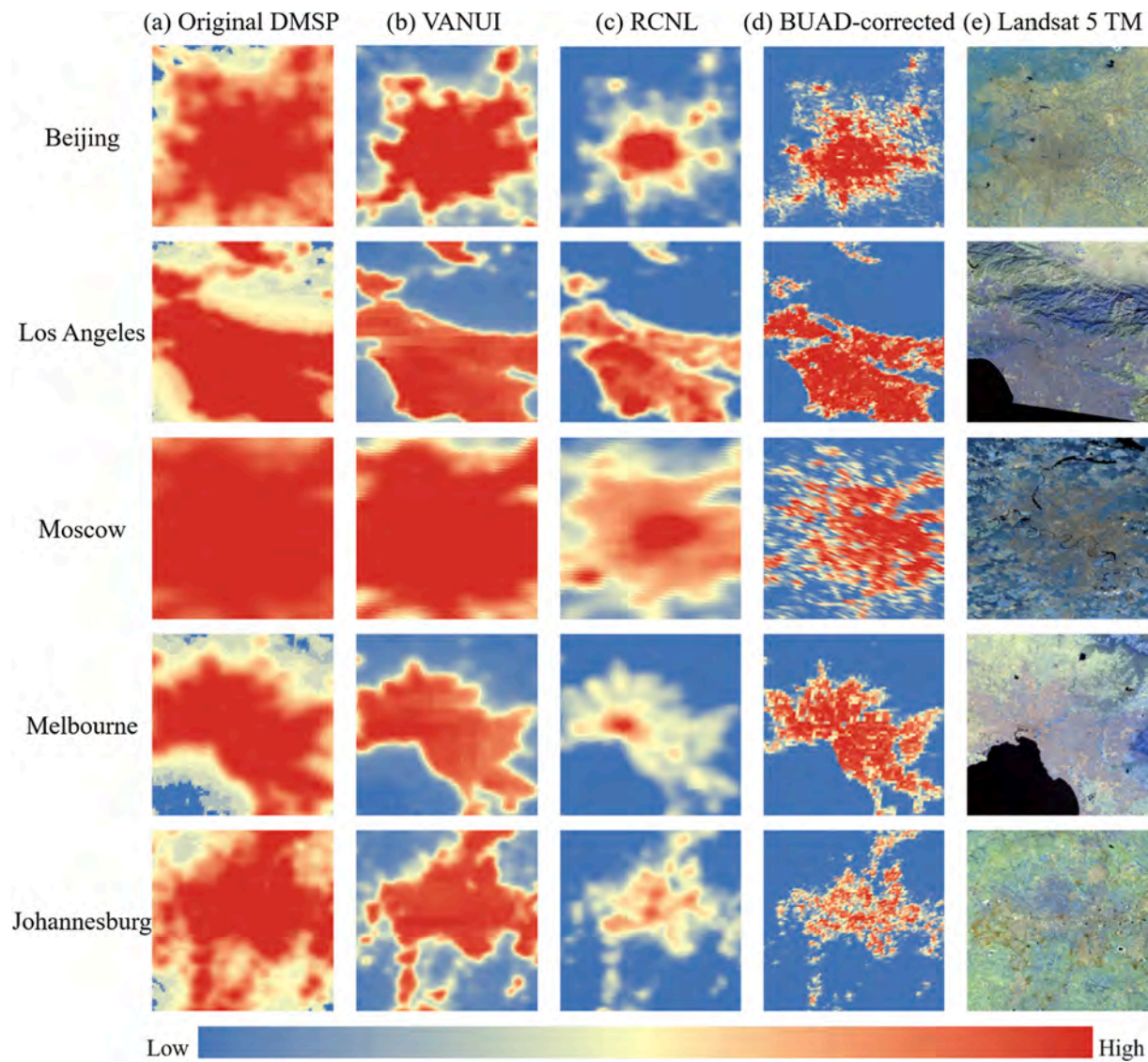


Fig. 4. Comparison between the original DMSP and the BUAD-corrected DMSP data in 2006 for the selected cities in reference to: (a) original DMSP data; and (b) VANUI (Vegetation Adjusted Normalized Urban Index) data; and (c) RCNL (radiance-calibrated nighttime light) data; and (d) saturation-corrected DMSP data using BUAD; and (e) Landsat 5 TM images (R: 7, G: 5, B: 4) in 2006.

gradually increasing during the study period, proving the reliability of our generated NTL product.

4.2. Evaluation of global EPC at different levels

For each country/district, optimal processing chain (including options in saturation correction, inter-annual correction, and regression model) was selected to estimate annual pixel-level EPC. The 24 processing chains were numbered sequentially, and the optimal one for each country/district in the world were displayed in Fig. 7, where 'No' + 'Backward' + 'Logarithmic' represents the processing chain consisting of the following options: no saturation correction in DMSP data, the backward inter-annual correction in DMSP/VIIRS data, and the logarithmic regression model to estimate EPC.

Through the proposed locally adaptive method, we produced the global EPC maps from 1992 to 2019, where the results for 1992, 2000, 2009, and 2019, as well as details for four typical regions, are presented in Fig. 8. The EPC estimates of another ten regions around the globe are shown in Fig. F1 of the Appendix. Please notice that the web link of full data is also available in the Appendix.

As mentioned above, the DMSP was calibrated using BUAD, taking

into account that vegetation surfaces are not always associated with urban areas. The visual comparison between Fig. 4(b) and Fig. 4(d) demonstrated the superiority of BUAD over NDVI when correcting DMSP. However, the effectiveness of BUAD in estimating EPC remained to be assessed. Therefore, we respectively compared ours with the one obtained from NDVI-corrected DMSP (hereafter referred to as NDVI's product) at the levels of globe, continent, and nation, according to the national EPC statistics.

4.2.1. Accuracy evaluation at the global level

Since the statistics provided by World Bank are only up to 2014, we accumulated the global EPC estimates for each year and then compared them with global statistics for the same year. Please notice that only the countries/districts with enough statistics during the study period were involved in the accuracy evaluation at the global level. Both the relative error (RE) and R^2 were adopted to conduct the evaluation per year. Table 2 shows that the EPC product based on BUAD achieved lower RE and high R^2 than the one based on NDVI for nearly all the years. Comparing the results for all the years combined, our average R^2 value (0.997) is higher than that of NDVI's (0.995). As for the mean of the absolute RE (i.e., MARE), our product also outperforms NDVI's with a

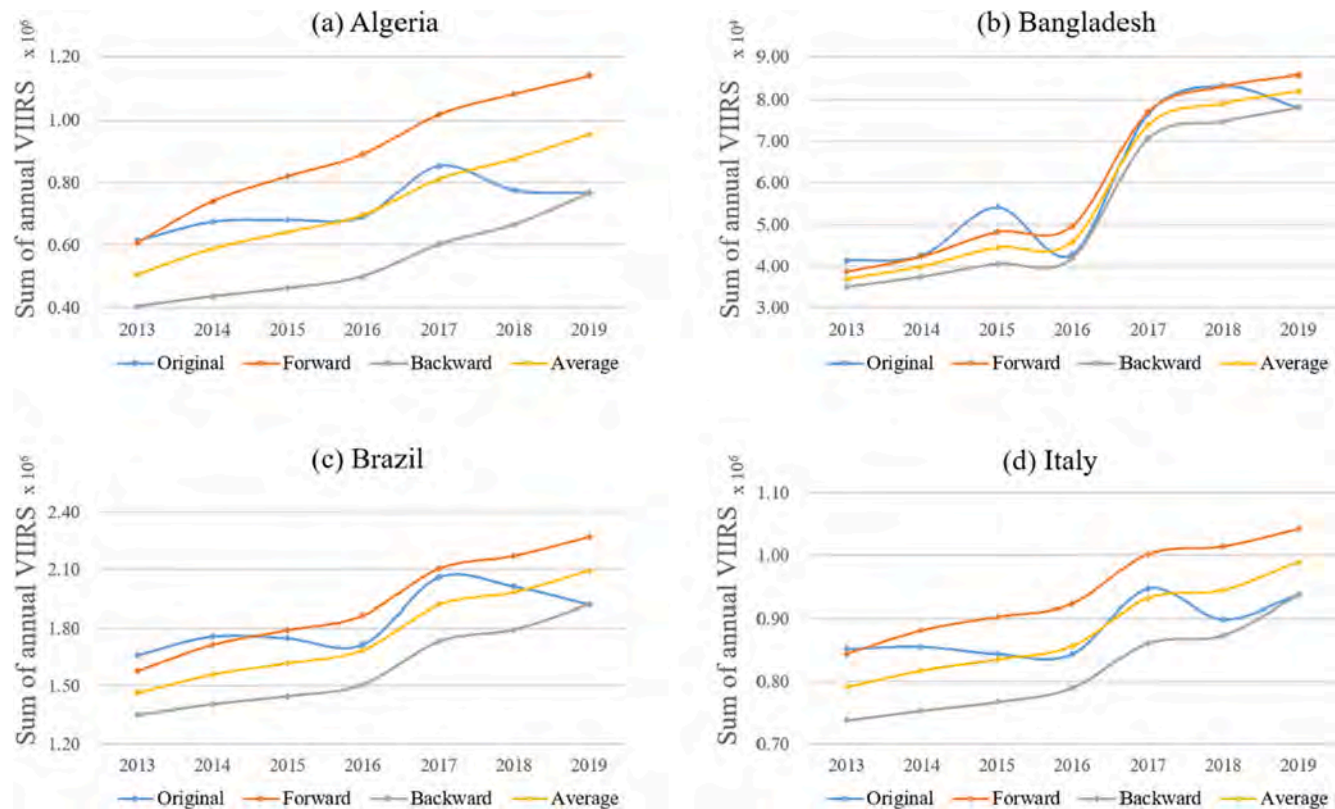


Fig. 5. Sums of annual VIIRS nighttime lights with different directions of inter-annual correction for the four selected countries.

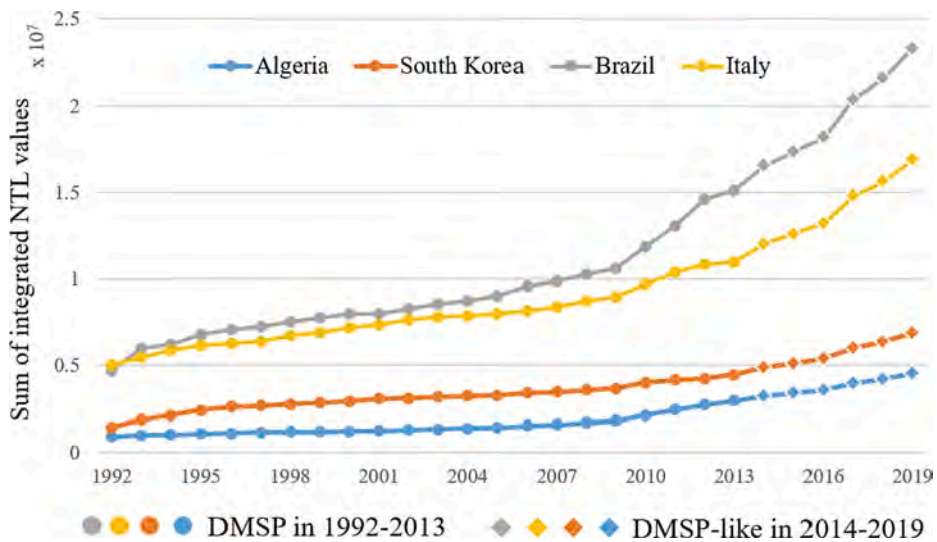


Fig. 6. The trend lines of the sum of integrated nighttime lights for the four selected countries from 1992 to 2019.

3.564% reduction in error.

From Table 2, we can observe that the estimated EPC values were generally lower than the statistical EPC in most years. It is likely due to the inability of nighttime light data to detect electric power consumption of all industries. The world (especially some developing countries such as China and India) underwent rapid urbanization and consumed a large amount of electric power, and some EPC occurred in the daytime would be ignored when using nighttime light as a proxy. The overestimation of EPC in 2013 could be attributed to the relatively high value of DMSP data after the inter-annual correction. Additionally, since the NTL data used in 2014 were the simulated DMSP from another kind

of NTL imagery (i.e., VIIRS), the regression-based error might account for the overestimation of EPC in 2014.

4.2.2. Accuracy evaluation at the continental level

Similar to the accuracy assessment at the global scale, we calculated the sum of EPC estimates of each continent (Antarctica excluded) year by year, and compared them with census data, to derive the RE values (Fig. 9). Similar patterns can be found between the curves of our product and those of NDVI's, especially in the North America. However, the RE values of our product are closer to 0 in most cases, with the greatest superiority occurring in Europe. Furthermore, the MARE values of both

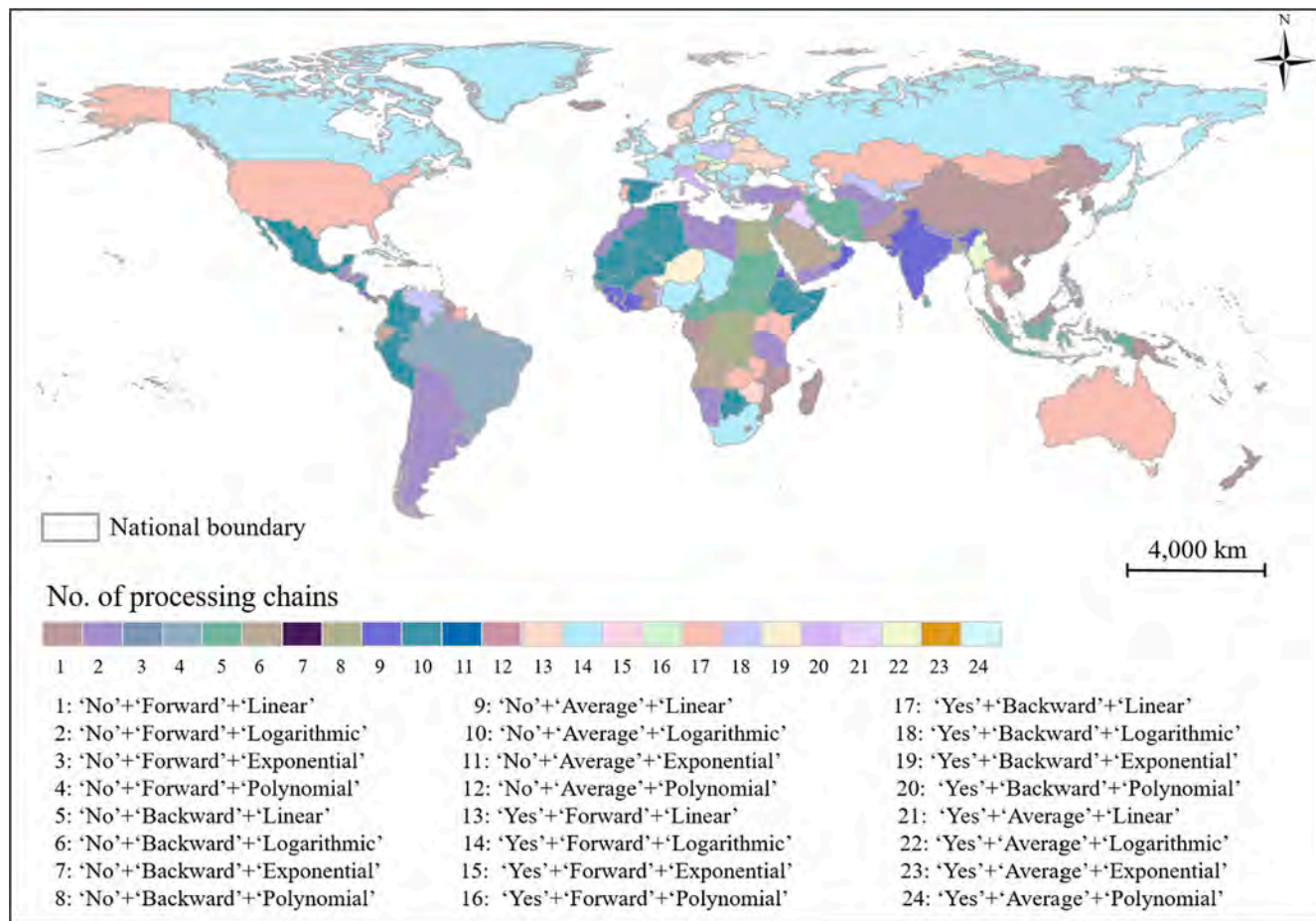


Fig. 7. The selected processing chain for each local country/district in the world. Note: the consistent NTL data were resampled to the pixel size of 1 km on Mollweide projection to facilitate calculation.

products are also listed in Fig. 9, showing that our BUAD-based product generally performs better than the one based on NDVI for all the continents, especially in Europe. This might be attributed to fact that the vegetation of Europe are not always inversely correlated with the urban surface.

4.2.3. Accuracy evaluation at the national level

The MARE criteria of model evaluation are listed in Table 3, according to Aydin [60]. Therefore, we respectively counted the number of countries/districts that fall into these four accuracy grades in our product and NDVI's, as shown in Fig. 10. For our EPC product, 68.15% of the countries/districts estimates are in the high-accuracy grade, compared to 57.04% for the NDVI's product. With regard to the grade of good estimation, our product (24.44%) also performs better than NDVI's (22.22%). For the other two grades, which are less satisfactory, the percentage of our product is only 7.41%, much lower than that of NDVI's (20.74%). The three countries with MARE values larger than 50% in our method are Finland, Iceland, and Norway, which are all located at high latitudes. The NTL data in high-latitude regions are susceptible to cloud coverage and aurora [40,52,61], which may account for the relatively inferior accuracy of these three countries.

4.3. Spatiotemporal dynamics of global EPC

4.3.1. Spatial distributions of global EPC map from 1992 to 2019

Based on the average EPC map during the whole study period, we investigated the areal percentage of the five EPC grades at the global, continental, and national levels, as displayed in Fig. 11. Globally, lighted

areas with low grade of EPC make up 51.70% of the total, while areas with relatively-high and high grades only account for 9.57%. At the continental level, low and relatively-low EPC grades occupy a considerable proportion in every continent, ranging from 55.71% (Europe) to 87.52% (South America). Medium EPC is more distributed in Europe than in other continents. The relatively-high EPC is less concentrated in South America (3.15%) and Africa (4.78%) than the other four continents. In terms of the areal percentage with high EPC level, Oceania (7.58%) and North America (5.93%) rank first and second, respectively, well above Africa (0.12%), which ranks last.

With regard to the national level, we selected the ten countries with the highest EPC statistics values in 2014 to explore the distributions of graded EPC. The lighted areas with low and relatively-low EPC grades respectively account for 79.08% and 73.60% of the total in Brazil and India, much higher than those percentages in South Korea (16.57%) and Russia Federation (16.02%). For the medium EPC level, the differences in areal percentage among the ten countries are not as significant as for the low and relatively-low EPC levels. The relatively-high EPC grade is more distributed in Russia Federation, France, South Korea, and Japan than in other six countries. With regard to the high EPC grade, there is no proportion in India, Russia Federation, Brazil, and France. Among the other six countries, Japan (19.33%), Canada (10.14%), and the United States (9.84%) rank in the top three.

4.3.2. Temporal variations of global EPC from 1992 to 2019

Fig. 12 shows the areal percentage of the five EPC grades at the global, continental, and national levels, based on the difference map between 1992 and 2019. From the perspective of global scale, the low-

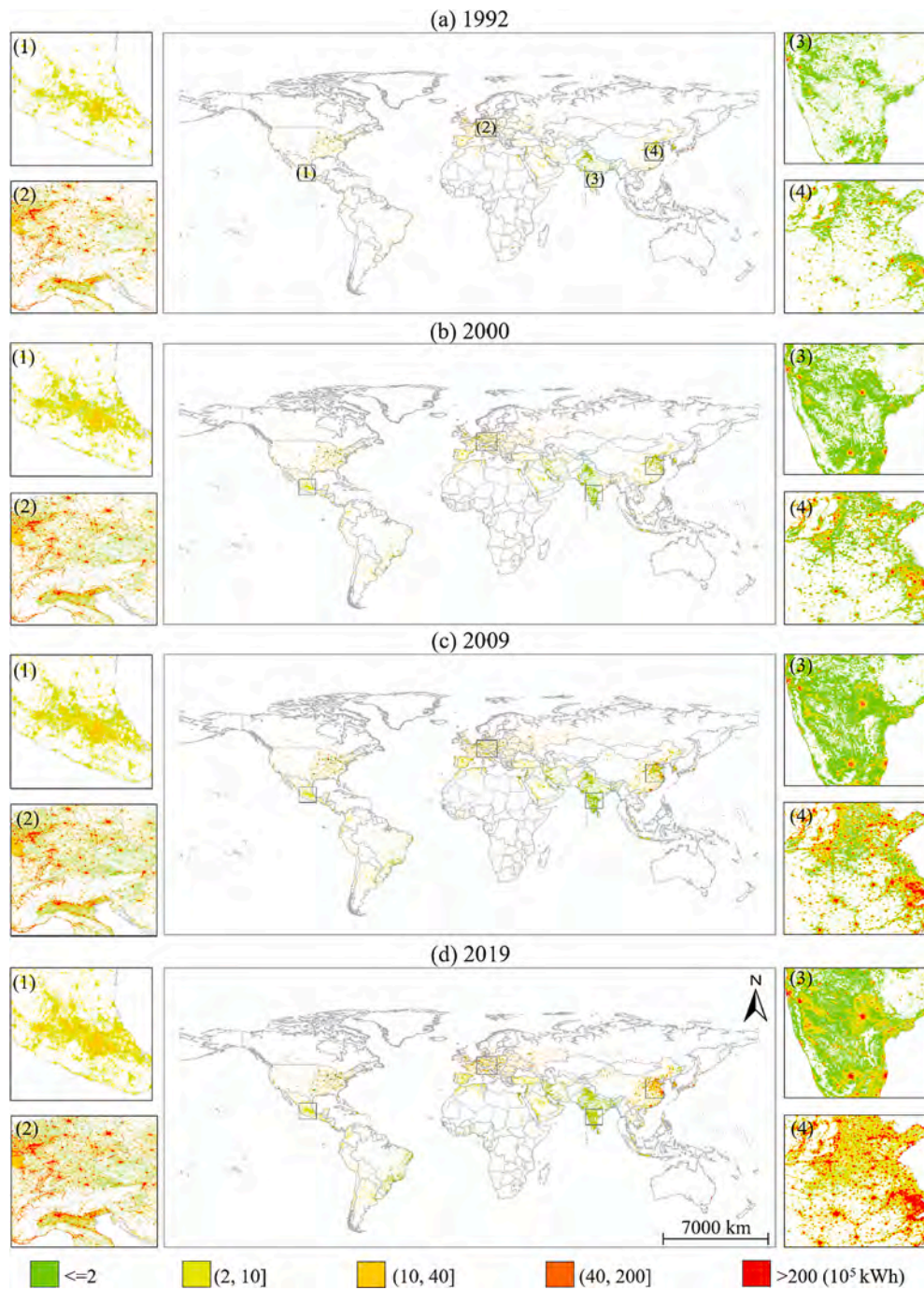


Fig. 8. The disaggregated global EPC maps for (a) 1992, (b) 2000, (c) 2009, and (d) 2019. Four typical sites, i.e., (1) Europe, (2) India, (3) China, and (4) Mexico, are selected as examples. Note: the consistent NTL data were resampled to the pixel size of 1 km on Mollweide projection to facilitate calculation.

growth grade occupies the largest areal percentage (42.81%), followed by the grades of no-obvious-growth, and moderate-growth. In the South America, most of the regions (84.20%) are in the classes of low-growth and no-obvious-growth, with only 0.33% in the high-growth class. The distribution in Africa is closely similar to South America. No-obvious-growth and low-growth EPC grades account for no less than 60% of each continent. A higher percentage of moderate-growth grade is distributed in Europe, compared to other continents. South America (5.21%) and Africa (6.56%) have lower areal ratio for relatively-high-growth level. Regarding the high-growth grade, the areal percentages in Asia, North America, and Oceania are well above those in South America and Africa.

At the national level, the lighted areas with no-obvious-growth grade

accounts for 69.12% of the total in Brazil, significantly higher than those in China (6.12%) and Russia Federation (6.20%). The areal percentage of low-growth grade varies from 14.51% (Brazil) to 55.31% (China). For the areal proportion of moderate-growth type, the top two countries are Russia Federation and France, whereas the bottom three countries are Brazil, India, and Canada. Relatively-high growth is observed in 26.04%, 19.73%, and 19.26% of the lighted areas in South Korea, Japan, and the United States, respectively. Area of high-growth EPC grade constitutes higher proportion in Japan, Canada, South Korea, and China than the other countries. In summary, large spatiotemporal variations in EPC were mainly observed in Japan, South Korea, the United States, and China, and small variations in Brazil and India.

Considering that the EPC estimates of 1992 tend to be biased in some

Table 2

Accuracy evaluation of our estimated global EPC product from 1992 to 2014.

Year	Statistical EPC(10^{12} kWh)	EPC Estimates		RE (%)		R^2	
		Ours	NDVI's	Ours	NDVI's	Ours	NDVI's
1992	11.11	10.70	9.10	-3.146%	-18.087%	0.990	0.981
1993	11.30	11.51	10.33	1.646%	-8.603%	0.994	0.985
1994	11.59	11.81	10.76	1.740%	-7.154%	0.997	0.991
1995	11.98	12.21	11.39	1.936%	-4.900%	0.998	0.993
1996	12.36	12.39	11.62	0.273%	-5.944%	0.998	0.994
1997	12.65	12.63	11.93	-0.135%	-5.718%	0.998	0.995
1998	12.93	12.93	12.28	-0.014%	-5.085%	0.998	0.995
1999	13.29	13.21	12.61	-0.574%	-5.117%	0.998	0.995
2000	13.89	13.61	13.12	-1.945%	-5.536%	0.997	0.995
2001	14.02	13.86	13.38	-1.101%	-4.554%	0.998	0.994
2002	14.51	14.32	13.89	-1.340%	-4.259%	0.996	0.992
2003	15.08	15.02	14.70	-0.396%	-2.531%	0.998	0.998
2004	15.74	15.38	15.14	-2.264%	-3.790%	0.999	0.999
2005	16.40	15.62	15.39	-4.841%	-6.196%	0.999	1.000
2006	17.08	16.11	15.91	-5.697%	-6.839%	0.999	0.999
2007	17.85	16.44	16.36	-7.948%	-8.338%	0.996	0.996
2008	18.21	16.88	16.93	-7.317%	-7.024%	0.996	0.996
2009	18.11	17.30	17.46	-4.503%	-3.607%	0.992	0.991
2010	19.39	18.60	19.14	-4.144%	-1.297%	0.999	0.997
2011	20.05	19.71	20.44	-1.754%	1.951%	0.999	0.997
2012	20.48	20.68	21.62	0.872%	5.558%	1.000	0.998
2013	21.13	22.24	23.39	5.155%	10.724%	0.997	0.998
2014	21.51	23.54	25.23	9.383%	17.282%	0.998	0.997
Average R^2		-	-	0.997	0.995		
MARE		2.962	6.526	-	-		

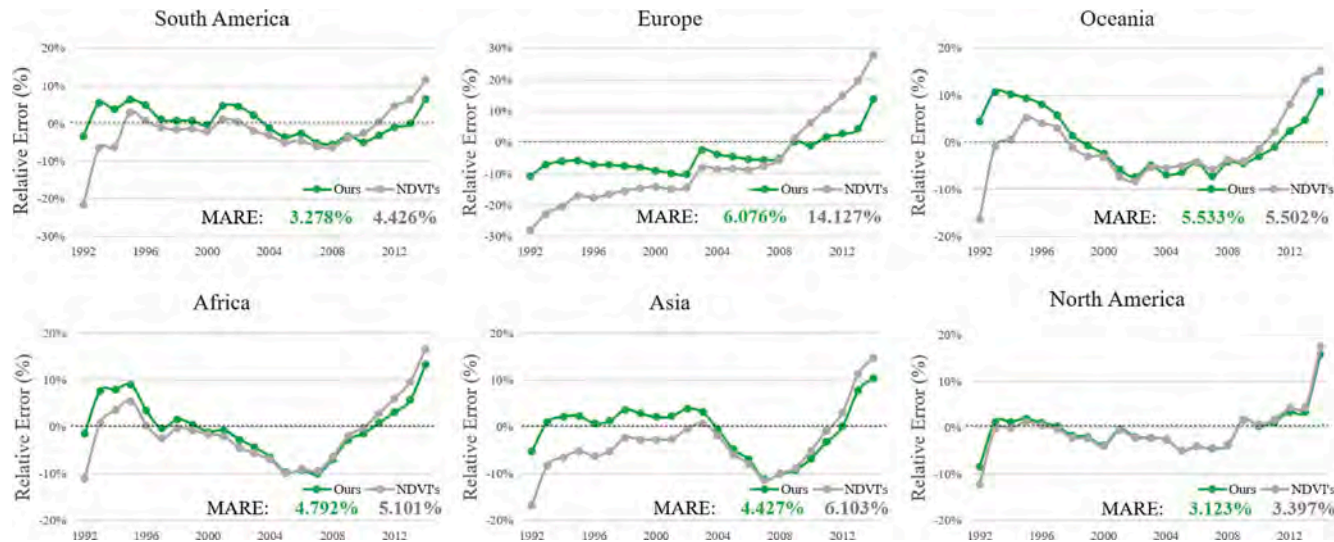


Fig. 9. Accuracy comparison between our product and the one from NDVI at the continental level for each year in 1992–2014. The dashed line in each subfigure denotes the case when RE is zero.

Table 3

The MARE criteria of model evaluation.

Value range (%)	Accuracy grade
(0, 10]	High-accuracy estimation
(10, 20]	Good estimation
(20, 50]	Reasonable estimation
(50, $+\infty$]	Inaccurate estimation

cases (Fig. 9), the temporal variation was also analyzed with the starting year of 1993. The relevant results are presented in the Appendix (Fig. F1), and it can be observed that the temporal patterns are almost the same as those in Fig. 12.

4.3.3. Spatial patterns of aggregated EPC maps from 2010 to 2019

The gridded EPC maps at the resolution of 1 km were aggregated to the provincial/state level, thus forming aggregated provincial EPC maps from 2010 to 2019. Firstly, global Moran's I was adopted to explore the spatial autocorrelation at the global, continental, and national scales, respectively. As Fig. 13(a) shows, positive spatial autocorrelations exist at the globe and each continents. The global Moran's I value of the world increased slightly from 2010 to 2013, and then remained relatively stable. Similarly, the global Moran's I values of all the six continents were also comparatively steady from 2010 to 2019. Oceania and North America were the top two continents in terms of the degree of spatial autocorrelation. Regarding the national scale, we took three countries (i.e., China, the United States, and India) as representatives to investigate. At this scale, the global Moran's I values were calculated based on the aggregated EPC of the Level 2 unit in GADM. The three countries

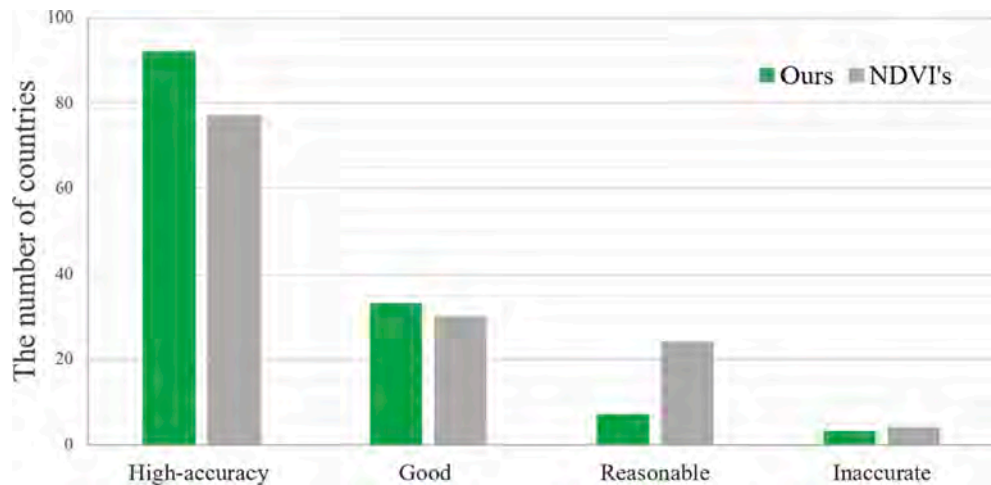


Fig. 10. National comparison between ours and NDVI's.

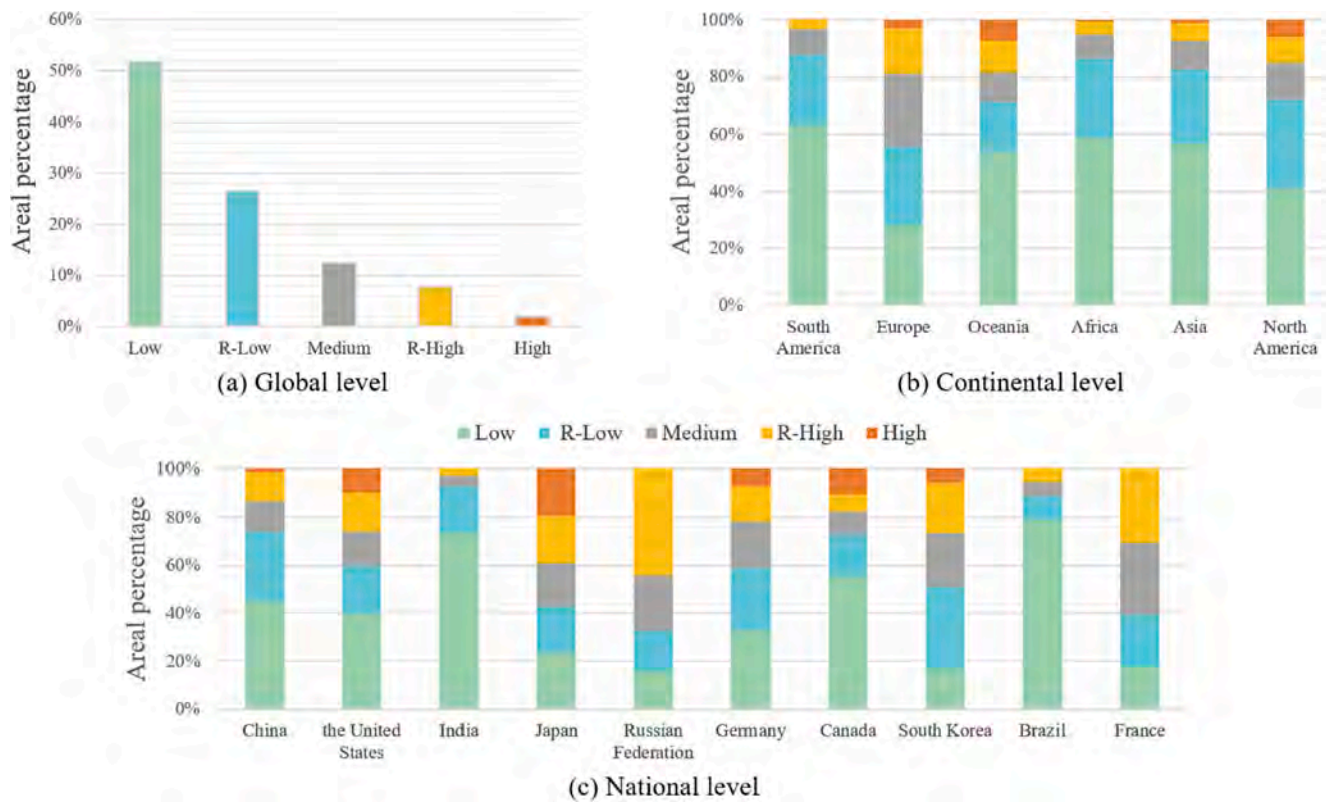


Fig. 11. Areal percentage of five EPC grades of average map from 1992 to 1919 at the (a) global, (b) continental, and (c) national levels, respectively.

presents diverse patterns, with the United States remaining stable, India showing a downward trend after 2013, and China consistently increasing until 2018. It is likely connected to the rapid urbanization in China during 2010–2019.

Secondly, we analyzed the spatial clustering patterns of aggregated provincial/state EPC maps for 2010 and 2019, respectively, using local Moran's I . From Fig. 14, it can be observed that the spatial clustering patterns have not changed greatly in this decade. Provinces/states belonging to High-High cluster type were found in China, India, Brazil, and North America, and Europe. The disappearing High-High type is mainly concentrated in western and southern Europe, indicating the decrease of EPC in these regions. Provinces/states exhibiting Low-Low pattern mainly appears in Africa, Southeast Asia, and North Europe. The Low-High cluster represents a pattern where the low EPC region are

surrounded by high EPC regions. Provinces/States with this type are largely located in Southeast Asia, North America, and Australia. The shift to Low-High cluster in 2019 occurred mainly in Vietnam, Laos, Mongolia, Canada, and Argentina, whose neighbors are the countries with significant electricity power consumption, such as China, the United States, and Brazil. In contrast to Low-High cluster, High-Low cluster indicates a high-EPC province/state encompassed by the low-EPC ones. No regions belongs to this category, which is possibly ascribed to the deepening globalization and urbanization.

4.3.4. Temporal dynamics of aggregated EPC maps from 2010 to 2019

Fig. 15 shows the global temporal dynamics divisions of the provincial/state-level aggregated EPC, according to the *SLOPE* index [57]. In the past decade, the provinces/states with rapid EPC growth are

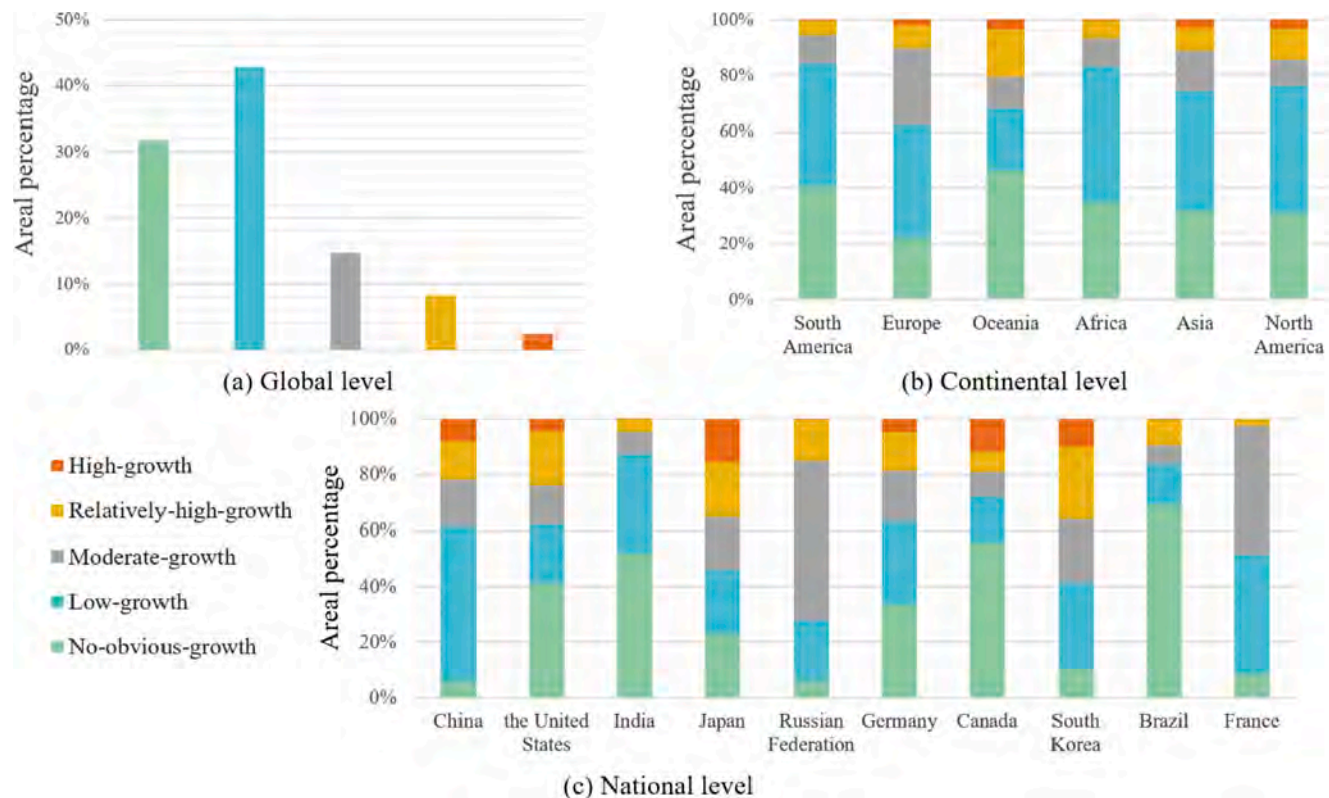


Fig. 12. Areal percentage of five EPC grades of growth map from 1992 to 2019 at the (a) global, (b) continental, and (c) national levels, respectively.

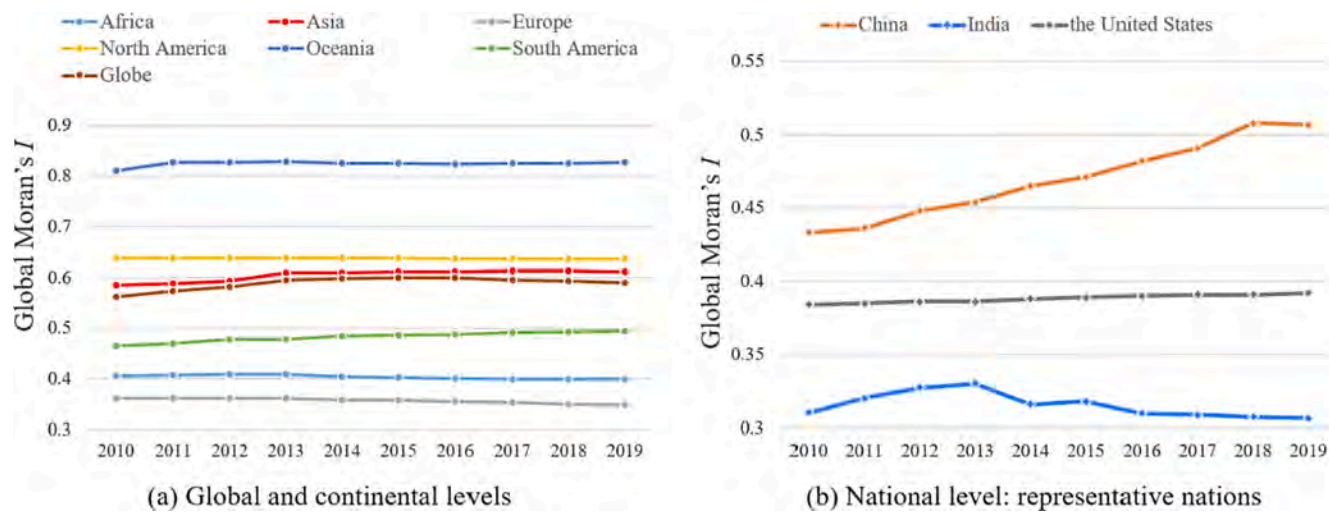


Fig. 13. Annual change of global Moran's I values for (a) provincial EPC at global and continental levels, and (b) prefectural-level EPC in three representative nations: China, India, and USA.

found in China, the United States, and Canada. As for the relatively-rapid growth type, these provinces are mainly concentrated in China. Besides, a few regions in Brazil, the United Kingdom, the United States, and Canada also witnessed relatively-rapid EPC growth. Provinces/states with moderate growth are in China, India, the United States, Canada, and Brazil. The distribution of relatively-slow growth is more widespread than those of the first three types. In terms of slow growth type, it is the most widely dispersed globally, with over 95% of provinces/states falling into to this grade. Almost all provinces/states of Africa did not witness significant EPC increase in the last decade.

5. Discussions

5.1. Comparison with EPC estimates based on other global NTL datasets

Several efforts have been made to produce global NTL datasets, which provide great opportunities for mapping global pixel-level EPC. For EPC estimates before 2014, properly calibrated DMSP NTL imagery is a practical choice. In our previous work [32], we adopted NDVI-corrected DMSP NTL data to estimate gridded EPC (hereafter referred to as NDdmsp). Results in Section 4.1 have proved that the advantage of BUAD-corrected DMSP over NDVI-corrected DMSP. Therefore, we adopted BUAD-corrected DMSP to obtain EPC estimates from 1992 to

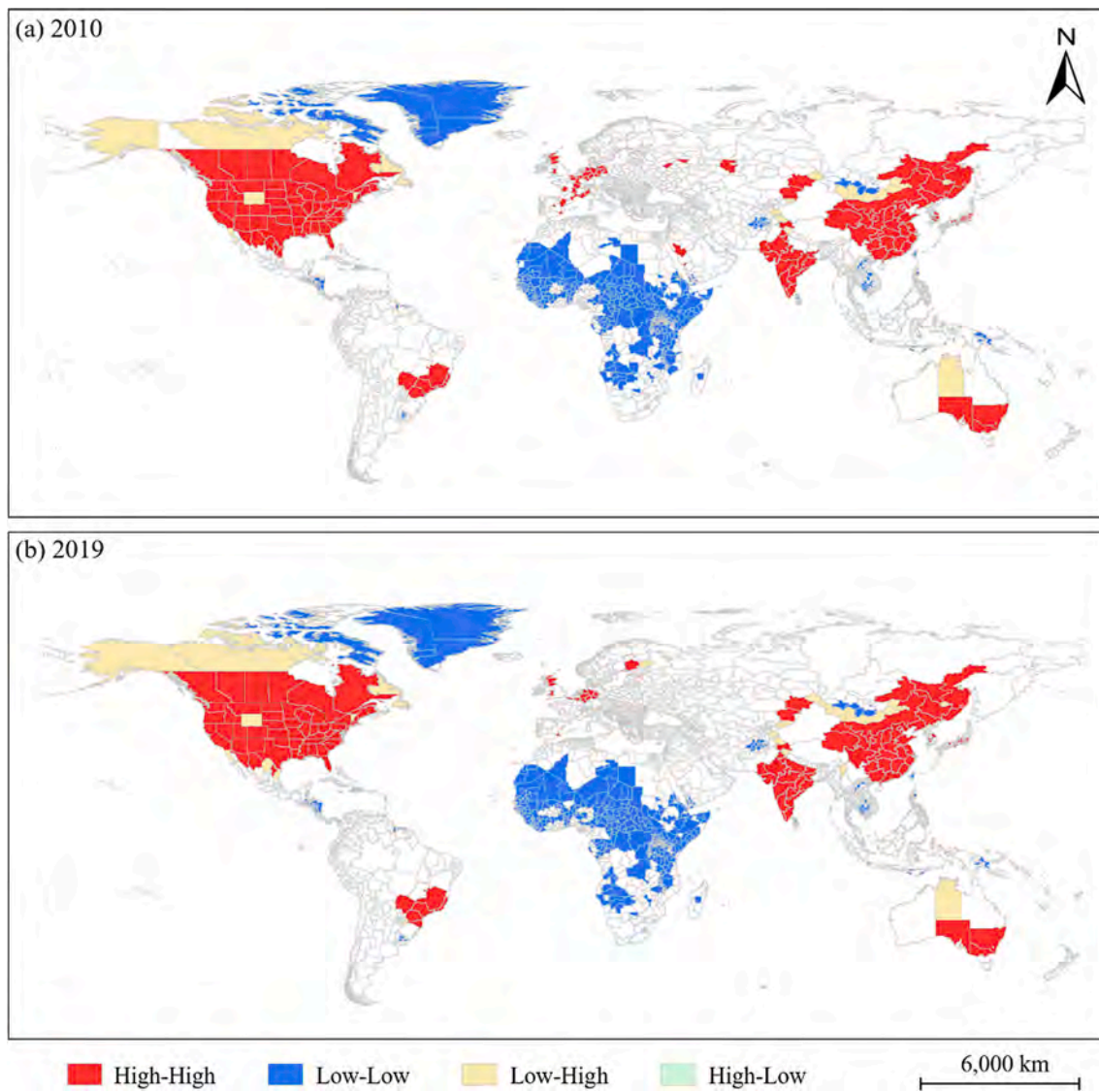


Fig. 14. Spatial clustering of neighborhood provinces/states in: (a) 2010 and (b) 2019 globally.

2013 (hereafter referred to as BUdmsp). The percentage of countries/districts in each accuracy grade is shown in Table 4. For the high-accuracy grade, the proportion of BUdmsp product is over 10% higher than that of NDdmsp. For grades with accuracy of good or higher (Grades I and II), the ratio of BUdmsp still performs better. In addition, the MARE values of BUdmsp at the global scale is 2.433%, lower than that of NDdmsp (3.011%). Therefore, the first contribution of this paper (i.e., the use of built-up area density to correct NTL images) still holds when only one type of nighttime light data (namely DMSP/OLS) is adopted to estimate EPC.

When it involves EPC estimates beyond 2014, the inclusion of VIIRS is necessary. Simulating DMSP-like NTL images based on VIIRS, Li et al. [40] published a harmonized global NTL dataset from 1992 to 2018. The values of their released DMSP-like data are the integers between 0 and 63. That is, the data range of their product is exactly the same as that of the original DMSP NSL data. Therefore, this global NTL dataset suffers from the same problems as the original DMSP NSL data, such as the saturation and inconsistency. Therefore, after removing the steps with VIIRS involved (i.e., Sections 3.1.1 and 3.1.2), we adopted the proposed method to estimate global pixel-level EPC maps (hereafter referred to as Li's product). Globally, the MARE value of EPC estimates is 10.18%, and only 57.04% of the countries/districts are in the grades of good or

higher. For the national scale, we compared the MARE values of Li's product with those of ours in China, India, the United States, and Canada (Table 5). It can be observed that our product achieves higher accuracies than Li's, especially in the developing countries (i.e., China and India). The authors stated there is uncertainty in their dataset for pixels with NTL intensities below 10. However, for a developing country like China, more than half of the pixels are below a luminance value of 10. Therefore, it can be inferred that the uncertainty of low-luminance pixels leads to a decrease in the accuracy of EPC estimation.

Recently, Chen et al. [41] released an extended time series (2000–2018) of global VIIRS-like NTL dataset with a spatial resolution of 500 m, based on deep learning method. To estimate EPC maps based on this dataset, our proposed method were modified as follows: 1) the choice about saturation correction was removed since this NTL dataset is VIIRS-like instead of DMSP-like; 2) the integration of DMSP and VIIRS was also canceled as this dataset has already been fused; 3) the pixel-level EPC maps were produced at the resolutions of 500 m and 1 km, respectively. For the results of 500-m-resolution, the global EPC estimates has a global MARE value of 11.97%, with only 47.14% of the countries reaching a high or good level. The accuracy of 1-km-resolution EPC estimates (hereafter referred to as Chen's product) is better than that of 500 m, with a MARE value of 10.22% globally and 65.92% of the

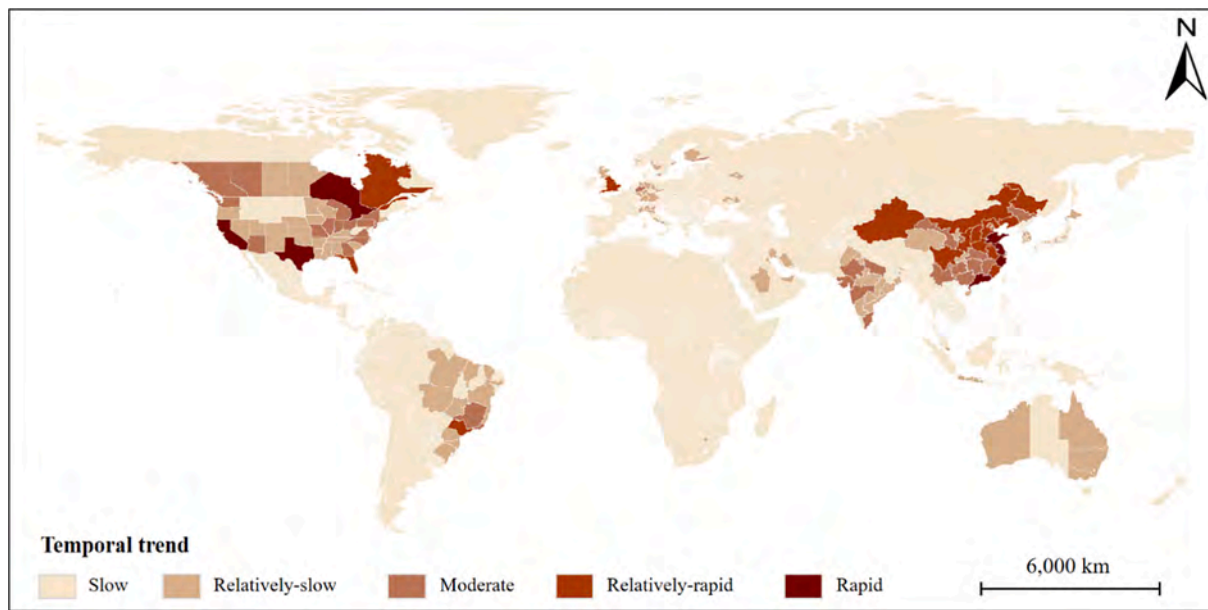


Fig. 15. Temporal dynamics types of the provincial/state-level EPC at the global scale from 2010 to 2019.

Table 4

Comparison of the percentages of countries/districts between BUdmsp and NDdmsp.

Accuracy grade	I	II	III	IV
	High-accuracy	Good	Reasonable	Inaccurate
BUdmsp	68.15%	22.96%	5.19%	3.70%
NDdmsp	57.78%	27.41%	11.11%	3.70%

Table 5

The MARE comparison between Li's and the number of countries/districts.

MARE values	Developing countries		Developed countries	
	China	India	The United States	Canada
Li's	17.49%	9.85%	3.74%	4.56%
Ours	7.25%	4.54%	3.18%	2.88%

countries achieving the grade of good or above. For the national scale, the MARE values of ours and Chen's product in the 10 countries with distinct geographical locations and urbanization levels were plotted in Fig. 16. It can be clearly observed that ours performs better than Chen's product at all the 10 countries, with the MARE decreasing by 3.4% to 13.5%. As Chen et al. stated, their method used 2012 median annual VIIRS data as one of the bases. However, the VIIRS images were only available from April 2012, leading to the median NTL intensity lower than usual level. This limitation may account for the relatively larger error in Chen's product.

5.2. Limitations and prospects

The utilization of built-up area density (BUAD) yielded better NTL data and higher-accuracy EPC estimates, compared with the results based on NDVI. This advantage is attributed to the fact that BUAD can more directly reflect the intensity of anthropogenic activities. Apparently, the accuracy of BUAD dataset would have an influence on final EPC estimates. Although the GISA we used in this work is by far the most accurate global impervious surface area product, a slightly higher omission error (5.16%) may lead to over-calibration of NTL in some omitted built-up areas. Furthermore, the accuracy performance of GISA varies around the world, which may also be a reason for the different

estimation errors of gridded EPC in each country/district [46]. It can be inferred that EPC estimates would be further improved if more accurate built-up area layer became available. Another future perspective is to consider the possibility that EPC could occur in some dark pixels of NTL imagery. For example, pixels with zero NTL intensity but non-zero BUAD are likely to experience EPC. Therefore, introducing a reasonable bias term in Eq. (1) could be a potential way.

To simulate pixel-level DMSP-like NTL data in 2014–2019, we firstly extended the inter-annual relationships of provincial aggregated VIIRS NTL to DMSP, and then transferred the relationships from the provincial scale to the pixel level. This two-step method does not take into account the different rates of NTL brightness change around the globe, and we will investigate the local adaptive scheme to alleviate this problem in the future. If sufficient post-2014 global EPC statistics are released, it will be possible to use only VIIRS to estimate gridded EPC, eliminating the necessity to integrate DMSP and VIIRS.

6. Conclusion

To gain an in-depth understanding of the up-to-date global EPC spatiotemporal dynamics, this research attempted to estimate pixel-level EPC product from 1992 to 2019 across the world, using two kinds of nighttime light (NTL) images, i.e., DMSP and VIIRS. Inspired by our previous work, this paper followed the method of local adaptive selection to model global EPC. Different from earlier approaches to the DMSP saturation effect, the built-up area density (BUAD) dataset was introduced to substitute NDVI. The advantage of BUAD-based correction lies in that the BUAD dataset has a higher spatial resolution and it is more directly related to human activities. Since the discontinuity problem that exists in DMSP are also present in VIIRS, we performed an inter-annual correction for time-series VIIRS data, with three directions (forward, backward, and average) considered. Another challenge to gain the time-series-extended EPC product is the integration of DMSP and VIIRS, because they differ significantly in NTL detection parameters. We designed a two-step regression-based scheme, which successively extended the inter-annual relationship of total provincial VIIRS NTL intensities to the temporal and spatial dimensions of DMSP, thus simulating DMSP-like images for 2014–2019. The 1-km-resolution global EPC product from 1992 to 2019 was modeled using the consistent global NTL dataset.

The results show that BUAD-based DMSP images present more

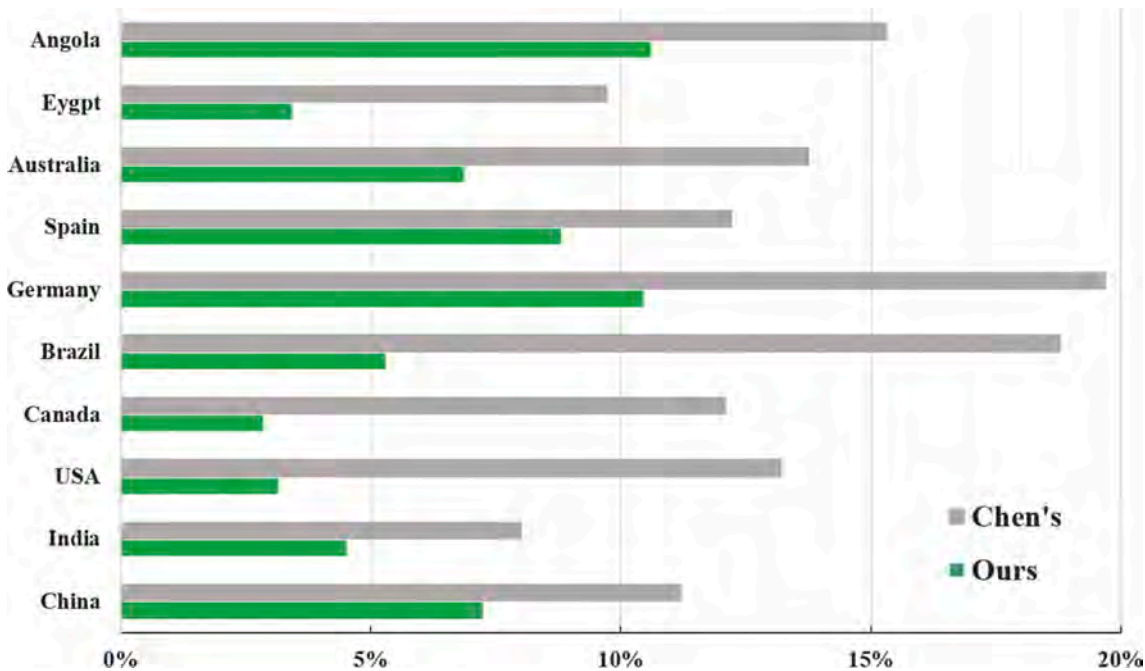


Fig. 16. The comparison of MARE values between Chen's and ours in the ten selected countries.

similar spatial patterns to the RCNL images when compared with the NDVI-based ones. The accuracy of our global EPC product was then evaluated using the NDVI-based estimates as a benchmark. Our generated maps achieve lower relative errors and higher R^2 from a global scale down to the national scales. Particularly, the proportion of countries/districts in the good-accuracy level or above in our product is 92.6%, obviously exceeding that of NDVI-based one (79.3%). Therefore, it can be concluded that our time-series-extended global EPC product is satisfactory. The spatiotemporal dynamics of EPC varied greatly across the globe. During 1992–2019, Japan, South Korea, and China experienced high areal percentages of high-growth category. In the recent decade, the degree of spatial autocorrelation did not change much globally as well as across continents, based on the aggregated provincial EPC. The spatial autocorrelation degree in India started to decrease since 2013, while that in China was still on the rise. In terms of the EPC growth rate from 2010 to 2019, China, the United States, and Canada are among the rapid-growth regions.

This pixel-level global EPC estimates from 1992 to 2019 provide a consistent and reliable perspective for investigating long-term human activities, making this time-series-extended global dataset indispensable and valuable. Furthermore, the detected spatiotemporal dynamics at multiple scales will deepen the understanding of regional differences in EPC, and serve as a scientific justification for the sustainable use of EPC worldwide.

Credit authorship contribution statement

Ting Hu: Methodology, Experiments, Writing – original draft. **Ting Wang:** Conceptualization, Methodology, Writing – review & editing. **Qingyun Yan:** Conceptualization, Writing – editing. **Tiexi Chen:** Visualization, Funding acquisition. **Shuanggen Jin:** Supervision, Funding acquisition. **Jun Hu:** Writing – revision.

Declaration of Competing Interest

The authors declare that they have no known competing financial interests or personal relationships that could have appeared to influence the work reported in this paper.

Data availability

Data will be made available online at <https://drive.google.com/drive/folders/1FzK7sSzOhYRNlXY5-y1SD-livRwyi3Fe?usp=sharing>.

Acknowledgements

The research was supported by the National Natural Science Foundation of China (41771069), Qian Xuesen Laboratory Space Exploration Experiment Cultivation Project (Grant No. TKTSPY-2020-06-02).

Appendix A. Supplementary material

Supplementary data to this article can be found online at <https://doi.org/10.1016/j.apenergy.2022.119473>.

References

- [1] Kapetanović M, Núñez A, van Oort N and Goverde RMP. Reducing fuel consumption and related emissions through optimal sizing of energy storage systems for diesel-electric trains. *Appl Energy* 2021;294: 117018.
- [2] Yang D, Luan W, Qiao L and Pratama M. Modeling and spatio-temporal analysis of city-level carbon emissions based on nighttime light satellite imagery. *Appl Energy* 2020;268:114696.
- [3] Al-mulali U, Binti Che Sab CN, Fereidouni HG. Exploring the bi-directional long run relationship between urbanization, energy consumption, and carbon dioxide emission. *Energy* 2012;46(1):156–67.
- [4] Liu L, Sun X, Chen C, Zhao E. How will auctioning impact on the carbon emission abatement cost of electric power generation sector in China? *Appl Energy* 2016; 168:594–609.
- [5] Mahalingam B, Orman WH. GDP and energy consumption: a panel analysis of the US. *Appl Energy* 2018;213:208–18.
- [6] Gambhir A, Napp TA, Emmott CJM, Anandarajah G. India's CO₂ emissions pathways to 2050: energy system, economic and fossil fuel impacts with and without carbon permit trading. *Energy* 2014;77:791–801.
- [7] Lean HH, Smyth R. CO₂ emissions, electricity consumption and output in ASEAN. *Appl Energy* 2010;87(6):1858–64.
- [8] Esmaeili P and Rafei M. Dynamics analysis of factors affecting electricity consumption fluctuations based on economic conditions: Application of SVAR and TVP-VAR models. *Energy* 2021;226: 120340.
- [9] Al-Garni AZ, Zubair SM, Nizami JS. A regression model for electric-energy-consumption forecasting in Eastern Saudi Arabia. *Energy* 1994;19:1043–9.
- [10] Shiu A, Lam P-L. Electricity consumption and economic growth in China. *Energy Policy* 2004;32(1):47–54.

- [11] Deng C, Lin W, Ye X, Li Z, Zhang Z, Xu G. Social media data as a proxy for hourly fine-scale electric power consumption estimation. *Environ. Plan. A: Econ. Space* 2018;50(8):1553–7.
- [12] Wang S, Liu X, Zhou C, Hu J, Ou J. Examining the impacts of socioeconomic factors, urban form, and transportation networks on CO₂ emissions in China's megalopolises. *Appl Energy* 2017;185:189–200.
- [13] Huang W, Ma D, Chen W. Connecting water and energy: assessing the impacts of carbon and water constraints on China's power sector. *Appl Energy* 2017;185:1497–505.
- [14] Parshall L, Gurney K, Hammer SA, Mendoza D, Zhou Y, Geethakumar S. Modeling energy consumption and CO₂ emissions at the urban scale: methodological challenges and insights from the United States. *Energy Policy* 2010;38(9):4765–82.
- [15] Amaral S, Câmara G, Monteiro AMV, Quintanilha JA, Elvidge CD. Estimating population and energy consumption in Brazilian Amazonia using DMSP night-time satellite data. *Comput Environ Urban Syst* 2005;29(2):179–95.
- [16] Pan J, Li J. Spatiotemporal dynamics of electricity consumption in China. *Appl. Spat. Anal. Pol.* 2017;1:28.
- [17] Shi K, Yu B, Huang Y, Hu Y, Yin B, Chen Z, et al. Evaluating the ability of NPP-VIIRS nighttime light data to estimate the gross domestic product and the electric power consumption of China at multiple scales: a comparison with DMSP-OLS data. *Remote Sens* 2014;6(2):1705–24.
- [18] Yeh C, Perez A, Driscoll A, Azzari G, Tang Z, Lobell D, et al. Using publicly available satellite imagery and deep learning to understand economic well-being in Africa. *Nat Commun* 2020;11(1).
- [19] Elvidge CD, Imhoff ML, Baugh KE, Hobson VR, Nelson I, Safran J, et al. Night-time lights of the world: 1994–1995. *ISPRS J Photogram Remote Sens* 2001;56(2):81–99.
- [20] Letu H, Nakajima TY, Nishio F. Regional-scale estimation of electric power and power plant CO₂ emissions using defense meteorological satellite program operational linescan system nighttime satellite data. *Environ Sci Technol Lett* 2014;1(5):259–65.
- [21] Townsend AC, Bruce DA. The use of night-time lights satellite imagery as a measure of Australia's regional electricity consumption and population distribution. *Int J Remote Sens* 2010;31(16):4459–80.
- [22] Zhao N, Ghosh T, Samson EL. Mapping spatio-temporal changes of Chinese electric power consumption using night-time imagery. *Int J Remote Sens* 2012;33(20):6304–20.
- [23] Cao X, Wang J, Chen J, Shi F. Spatialization of electricity consumption of China using saturation-corrected DMSP-OLS data. *Int J Appl Earth Obs Geoinf* 2014;28:193–200.
- [24] He C, Ma Q, Liu Z, Zhang Q. Modeling the spatiotemporal dynamics of electric power consumption in Mainland China using saturation-corrected DMSP/OLS nighttime stable light data. *Int J Digital Earth* 2014;7(12):993–1014.
- [25] Jasinski T. Modeling electricity consumption using nighttime light images and artificial neural networks. *Energy* 2019;179:831–42.
- [26] Xie Y, Weng Q. Detecting urban-scale dynamics of electricity consumption at Chinese cities using time-series DMSP-OLS (Defense Meteorological Satellite Program-Operational Linescan System) nighttime light imageries. *Energy* 2016;100:177–89.
- [27] Shi K, Chen Y, Yu B, Xu T, Yang C, Li L, et al. Detecting spatiotemporal dynamics of global electric power consumption using DMSP-OLS nighttime stable light data. *Appl Energy* 2016;184:450–63.
- [28] Xiao H, Ma Z, Mi Z, Kelsey J, Zheng J, Yin W, et al. Spatio-temporal simulation of energy consumption in China's provinces based on satellite night-time light data. *Appl Energy* 2018;231:1070–8.
- [29] Lu L, Weng Q, Xie Y, Guo H and Li Q. An assessment of global electric power consumption using the Defense Meteorological Satellite Program-Operational Linescan System nighttime light imagery. *Energy* 2019;189: 116351.
- [30] Li S, Cheng L, Liu X, Mao J, Wu J and Li M. City type-oriented modeling electric power consumption in China using NPP-VIIRS nighttime stable light data. *Energy* 2019;189: 116040.
- [31] Wang J, Lu F. Modeling the electricity consumption by combining land use types and landscape patterns with nighttime light imagery. *Energy* 2021;234:121305.
- [32] Hu T, Huang X. A novel locally adaptive method for modeling the spatiotemporal dynamics of global electric power consumption based on DMSP-OLS nighttime stable light data. *Appl Energy* 2019;240:778–92.
- [33] Zhang W, Robinson C, Guhathakurta S, Garikapati VM, Dilksina B, Brown MA, et al. Estimating residential energy consumption in metropolitan areas: a microsimulation approach. *Energy* 2018;155:162–73.
- [34] Shi K, Huang C, Yu B, Yin B, Huang Y, Wu J. Evaluation of NPP-VIIRS night-time light composite data for extracting built-up urban areas. *Remote Sens Lett* 2014;5(4):358–66.
- [35] Jeswani R, Kulshrestha A, Gupta PK, Srivastav S. Evaluation of the consistency of DMSP-OLS and SNPP-VIIRS Night-time Light Datasets. *J Geomat* 2019;13:98–105.
- [36] Zhu X, Ma M, Yang H, Ge W. Modeling the spatiotemporal dynamics of gross domestic product in China using extended temporal coverage nighttime light data. *Remote Sens* 2017;9:626.
- [37] Li Xi, Li D, Xu H, Wu C. Intercalibration between DMSP/OLS and VIIRS night-time light images to evaluate city light dynamics of Syria's major human settlement during Syrian Civil War. *Int J Remote Sens* 2017;38(21):5934–51.
- [38] Zheng Q, Weng Q, Wang K. Developing a new cross-sensor calibration model for DMSP-OLS and Suomi-NPP VIIRS night-light imageries. *ISPRS J Photogram Remote Sens* 2019;153:36–47.
- [39] Zhao M, Zhou Y, Li X, Zhou C, Cheng W, Li M, et al. Building a Series of Consistent Night-Time Light Data (1992–2018) in Southeast Asia by Integrating DMSP-OLS and NPP-VIIRS. *IEEE Trans Geosci Remote Sens* 2020;58(3):1843–56.
- [40] Li X, Zhou Y, Zhao M, Zhao X. A harmonized global nighttime light dataset 1992–2018. *Sci Data* 2020;7:1–9.
- [41] Chen Z, Yu B, Yang C, Zhou Y, Yao S, Qian X, et al. An extended time series (2000–2018) of global NPP-VIIRS-like nighttime light data from a cross-sensor calibration. *Earth Syst Sci Data* 2021;13(3):889–906.
- [42] Huang X, Hu T, Li J, Wang Q, Benedictsson JA. Mapping urban areas in China using multisource data with a novel ensemble SVM method. *IEEE Trans Geosci Remote Sens* 2018;56(8):4258–73.
- [43] Schneider A, Friedl M A and Potere D. A new map of global urban extent from MODIS satellite data. *Environ Res Lett* 2009;4: 044003.
- [44] Liu X, Hu G, Chen Y, Li X, Xu X, Li S, et al. High-resolution multi-temporal mapping of global urban land using Landsat images based on the Google Earth Engine Platform. *Remote Sens Environ* 2018;209:227–39.
- [45] Gong P, Li X, Wang J, Bai Y, Chen B, Hu T, et al. Annual maps of global artificial impervious area (GAIA) between 1985 and 2018. *Remote Sens Environ* 2020;236: 111510.
- [46] Huang X, Li J, Yang J, Zhang Z, Li D, Liu X, et al. to 2019. *Science China Earth Sci* 1972;2021:1–12.
- [47] Ma T, Zhou C, Pei T, Haynie S, Fan J. Responses of Suomi-NPP VIIRS-derived nighttime lights to socioeconomic activity in China's cities. *Remote Sens Lett* 2014;5(2):165–74.
- [48] Lv Q, Liu H, Wang J, Liu H and Shang Y. Multiscale analysis on spatiotemporal dynamics of energy consumption CO₂ emissions in China: Utilizing the integrated of DMSP-OLS and NPP-VIIRS nighttime light datasets. *Sci Total Environ* 2020;703: 134394.
- [49] Wu J, Wang Z, Li W, Peng J. Exploring factors affecting the relationship between light consumption and GDP based on DMSP/OLS nighttime satellite imagery. *Remote Sens Environ* 2013;134:111–9.
- [50] Zhao J, Ji G, Yue YanLin, Lai Z, Chen Y, Yang D, et al. Spatio-temporal dynamics of urban residential CO₂ emissions and their driving forces in China using the integrated two nighttime light datasets. *Appl Energy* 2019;235:612–24.
- [51] Huang X, Cao Y and Li J. An automatic change detection method for monitoring newly constructed building areas using time-series multi-view high-resolution optical satellite images. *Remote Sens Environ* 2020;244: 111802.
- [52] Román MO, Wang Z, Sun Q, Kalb V, Miller SD, Molthan A, et al. NASA's Black Marble nighttime lights product suite. *Remote Sens Environ* 2018;210:113–43.
- [53] Li X, Ma R, Zhang Q, Li D, Liu S, He T, et al. Anisotropic characteristic of artificial light at night – Systematic investigation with VIIRS DNB multi-temporal observations. *Remote Sens Environ* 2019;233: 111357.
- [54] Ma T, Zhou C, Pei T, Haynie S, Fan J. Quantitative estimation of urbanization dynamics using time series of DMSP/OLS nighttime light data: A comparative case study from China's cities. *Remote Sens Environ* 2012;124:99–107.
- [55] Ord JK. Spatial processes. *Encyclopedia of Statistical Sciences* 2004;12.
- [56] Anselin L. Local indicators of spatial association—LISA. *Geographical analysis* 1995;27:93–115.
- [57] He C, Ma Q, Li T, Yang Y, Liu Z. Spatiotemporal dynamics of electric power consumption in Chinese Mainland from 1995 to 2008 modeled using DMSP/OLS stable nighttime lights data. *J Geog Sci* 2012;22(1):125–36.
- [58] Zhang Q, Schaaf C, Seto KC. The vegetation adjusted NTL urban index: A new approach to reduce saturation and increase variation in nighttime luminosity. *Remote Sens Environ* 2013;129:32–41.
- [59] Cao Z, Wu Z, Kuang Y, Huang N, Wang M. Coupling an intercalibration of radiance-calibrated nighttime light images and land use/cover data for modeling and analyzing the distribution of GDP in Guangdong. *China Sustain* 2016;8:108.
- [60] Aydin G. Modeling of energy consumption based on economic and demographic factors: the case of Turkey with projections. *Renew Sustain Energy Rev* 2014;35: 382–9.
- [61] Zhang Q, Pandey B, Seto KC. A robust method to generate a consistent time series from DMSP/OLS nighttime light data. *IEEE Trans Geosci Remote Sens* 2016;54(10):5821–31.